



With the support of the
Erasmus+ Programme
of the European Union



Determination of the Ice Floe Characteristics Resulting From a Non-Typical Ice Breaking Bow Shape and Level Ice Interactions

Submitted on : 25 September 2020

Handed in by: Yusuf Sefa Özhan
Rumpffsweg 13, 20537 Hamburg
yusufsefaozhan@gmail.com

Enrolment number: 219 200 012

Supervisors: Dr. Daniela Myland
Quentin Hisette

First Reviewer: Prof. Dr. Antonio Crucelaegui
Universidad Politécnica de Madrid
Avenida de la Memoria 4, 28040 Madrid,
Spain

Second Reviewer: Prof. Dr. Robert Bronsart
Universität Rostock
Albert – Einstein Straße 2, 18059 Rostock,
Germany



This work is licensed under a Creative Commons Attribution 4.0 International License.

DECLARATION OF AUTHORSHIP

I, **Yusuf Sefa ÖZHAN**, declare that this thesis and the work presented in it are my own and have been generated by me as the result of my own original research.

Where I have consulted the published work of others, this is always clearly attributed.

Where I have quoted from the work of others, the source is always given. With the exception of such quotations, this thesis is entirely my own work.

I have acknowledged all main sources of help.

Where the thesis is based on work done by myself jointly with others, I have made clear exactly what was done by others and what I have contributed myself.

This thesis contains no material that has been submitted previously, in whole or in part, for the award of any other academic degree or diploma.

I cede copyright of the thesis in favour of the University of Rostock.

Hamburg, September 25, 2020

Signature:

This page is intentionally left blank.

ABSTRACT

As the impact of climate change has been felt increasingly in polar regions, trends and needs in marine traffic have been updated in parallel with these changes as well. Due to the decrease in sea ice extent and in ice thickness, new routes have started to be taken into consideration for marine traffic. This accessibility resulted in increasing number and variety of vessels entering Arctic and Antarctic waters in last decades. In addition to the icebreakers and fishing vessels already in operable in these areas, cruise and military vessels have also started to increase their activities in these regions.

This aforementioned demand emerging in recent years results in a need for better understanding of the interaction between sea ice and the vessels having conventional bow shape. In fact, hull - sea ice interaction processes are well understood for typical icebreaker vessels with inclined bow and low flare angles. However, non-typical ice-breaking vessels bring some unknown phenomena as they move across the sea ice. Shedding light on these unclear matters, the design processes of such vessels can be optimized as well as their operability can be determined in more efficient way.

With the support of Office of Naval Research (ONR), a research project was prepared at HSVA in order to conduct the experimental investigations regarding the level ice resistance of ships with non-typical ice-breaking bow shapes. A ship model taking DTMB 5415 geometry as reference has been manufactured by HSVA with this purpose in mind.

In the course of this thesis visual observations based on the underwater recordings made during level ice resistance experiments are performed. By doing these observations, it was aimed to improve the understanding of the ice breaking process for this particular ship model having unconventional bow shape and to compare these observations with the experimental results.

This page is intentionally left blank.

Contents

ABSTRACT	v
List of Figures	ix
List of Tables	xii
1 INTRODUCTION	1
1.1 Typical and non-typical ice-breaking ships	3
1.2 Image analysis in Arctic technology	10
1.3 Ice model tests in Arctic technology	12
1.4 The aim of the study	15
2 METHODOLOGY	16
2.1 Experimental setup and input variables	16
2.1.1 Ship model presented for the research	17
2.1.2 Test parameters	19
2.1.3 Recording the test runs	22
2.2 Decision making on using the python and the scientific library	23
2.3 Developing the algorithm and implementation	24
2.3.1 Image pre-processing	29
2.3.2 Image segmentation and morphological operations	31
2.3.3 User interface built to ease the parameter determination	37
2.4 Composing the input data to be analyzed	38
2.4.1 Extraction and classification of the images that can be analyzed	38
2.5 Obtained physical properties from image segmentation	41
2.6 Conversion of the pixel based values into the metric system	46
2.7 Convergence study regarding number of the images to be evaluated	49
2.8 Exclusion of incoherent ice floes from the outputs	50
2.9 Limitations	53
3 RESULTS	55
3.1 Correlation of ice floe characteristics on test variables	55
3.1.1 Correlation between ice floe characteristics and model speed	55
3.1.2 Correlation between ice floe characteristics and level ice thickness	59
3.1.3 Correlation between ice floe characteristics and hull angle	63

3.1.4	Ice coverage around bow section	67
3.2	Associating the ice floe characteristics with the bow resistance measured on the model	69
3.2.1	Relation between ice floe characteristics, bow resistance and level ice thickness	69
3.2.2	Relation between ice floe characteristics, bow resistance and speed	73
4	CONCLUSION	75
5	FUTURE IMPROVEMENTS	77
6	ACKNOWLEDGEMENTS	78
	REFERENCES	79

List of Figures

1.1	Sea ice concentration (% , shades of blue) and thickness (labeled contours) during the navigation period (June–October). Model 2010–2019 (a) and 2030–2039 (b)	2
1.2	A polar class icebreaker Kapitan Khlebnikov as it moves accross the sea ice [5]	4
1.3	The forces present when a ship is proceeding in ice, Riska, The Encyclopedia of Maritime and Offshore Engineering, 2017 [8]	6
1.4	The nature of ice resistance as an average longitudinal force, Riska, Design of ice breaking ships [4]	7
1.5	Visual comparison between conventional and non conventional bow shaped vessels	9
1.6	Definition of hull angles [14]	10
1.7	Evaluation of an image taken by an UAV and used for sea ice floe properties [15]	11
1.8	Stitched underwater images (on top) and analyzed image with identified ice floes (on bottom) [16]	12
1.9	HSVA’s large ice model basin [17]	13
1.10	Level ice model test at HSVA	14
2.1	Hull lines of the reference ship DTMB 5415 [19]	17
2.2	Instruments installed along the model [19]	19
2.3	Side picture of the model at HSVA’s workshop	19
2.4	Top view of the model as it is towing by the carriage	22
2.5	Underwater and front camera snapshots of the model	23
2.6	Counting bacteria in petri dish using Python [21]	24
2.7	Grayscale and RGB channels representation [22]	25

2.8	Edge definition and close look on ice floe edges	27
2.9	Algorithm tree	28
2.10	Input and output images processed in the first module,	30
2.11	Watershed approach in region based segmentation [24]	32
2.12	An example image with an object in it and its distance function [25] . . .	32
2.13	Segmentation steps and resulting regions representing broken ice floes . .	34
2.14	Histogram of the segmented grayscale image	35
2.15	Final output images	37
2.16	User interface for edge detection	38
2.17	Time intervals corresponding to model speeds tested	39
2.18	Synchronization signals installed on the model	40
2.19	Printed information of ice floes for analyzed images	42
2.20	Checkered pattern on the model	47
2.21	Pixel measurement representation	48
2.22	Convergence behavior in mean ice floe sizes as number of the images ana- lyzed increases	49
2.23	Standard deviation in mean ice floe sizes as number of the images analyzed increases	50
2.24	Checking the ice floes manually around image borderline	52
2.25	Tiny ice particles formed along bow region as model crushes the level ice sheet	54
3.1	Correlation between mean ice floe size and model speed	56
3.2	Correlation between ice floe number and model speed	58
3.3	Correlation between mean ice floe size and level ice thickness	60
3.4	Correlation between ice floe density and level ice thickness	62
3.5	Limiting lines for hull angles to be shown	64
3.6	Correlation between mean ice floe size and normal angles	65
3.7	Sample comparison of the greatest ice floes formed between lower and higher draughts	66
3.8	Correlation between ice floe densities and normal angles	67
3.9	Ice coverage dependency over level ice thickness values tested	68

3.10 Bow resistance - mean ice floe size relation depending on level ice thickness, $T = 5.15 \text{ m}$	70
3.11 Bow resistance - mean ice floe size relation depending on level ice thickness, $T = 10.15 \text{ m}$	72
3.12 Bow resistance - ice coverage depending on model speed, $T = 5.15 \text{ m}$. .	73
3.13 Bow resistance - ice coverage depending on model speed, $T = 10.15 \text{ m}$.	74

List of Tables

- 2.1 DTMB 5415 ship characteristics 17
- 2.2 Target values for level ice properties 20
- 2.3 Draught values, in full scale 20
- 2.4 Test matrix, in full scale 21
- 2.5 Image range that can be analysed within time intervals to be considered . 41
- 2.6 Conversion to real scale, from pixel length to mm 48
- 2.7 Conversion to real scale, from pixel² to mm² 48

- 3.1 Mean normal angles corresponding to the delimiter 1 and 2 64
- 3.2 *R – squared* values for the linear regression performed 73

Notations

Greek symbols

α Waterline angle

λ Scaling factor

ϕ Buttock angle

ψ Normal angle

Abbreviations

2D Two-dimensional

3D Three-dimensional

HD High Definition

HSVA Hamburgische Schiffbau-Versuchsanstalt, Hamburg Ship Model Basin

RGB Red, green, blue

ROI Region of interest

UAV Unmanned aerial vehicle

Roman symbols

B Ship breadth

E Modulus of elasticity

g Gravitational acceleration

H Level ice thickness

L_{pp} Ship length between perpendiculars

L_{wl} Maximum beam at waterline

L_{wl}	Waterline length
T	Ship draught
V	Ship speed

Chapter 1

INTRODUCTION

As the effects of global warming have been becoming more and more visible, increasing number of researches offering an insight into what actually awaits our planet. Although many of those effects appeared to be irreversible, a great number of actions are being taking against climate change by societies, governmental and non governmental organizations in order to slow down the course of events. Arctic and Antarctic regions are put in the center of those actions, knowing the fact that are more sensitive to global warming and have been more affected than other regions. According to the researches, it is observed over last decades that the sea ice extent and thickness have shrunk drastically. Furthermore, a projection study based on the linear trend of the last 20 years of data shows that the first Arctic ice-free summer year will take a place at 2036. Another projection made based on the trend over the last 30 years shows that the first Arctic ice-free summer is forecasted to be 12 years later than first condition [1].

Those changes and actions aforementioned are of particular concern to maritime activities and to shipping industry. As the increase in sea ice-free regions and the weakening the severe ice conditions in the Arctic and Antarctic waters, more amount and type of vessels have been entering those regions and resulting in escalated maritime traffic.

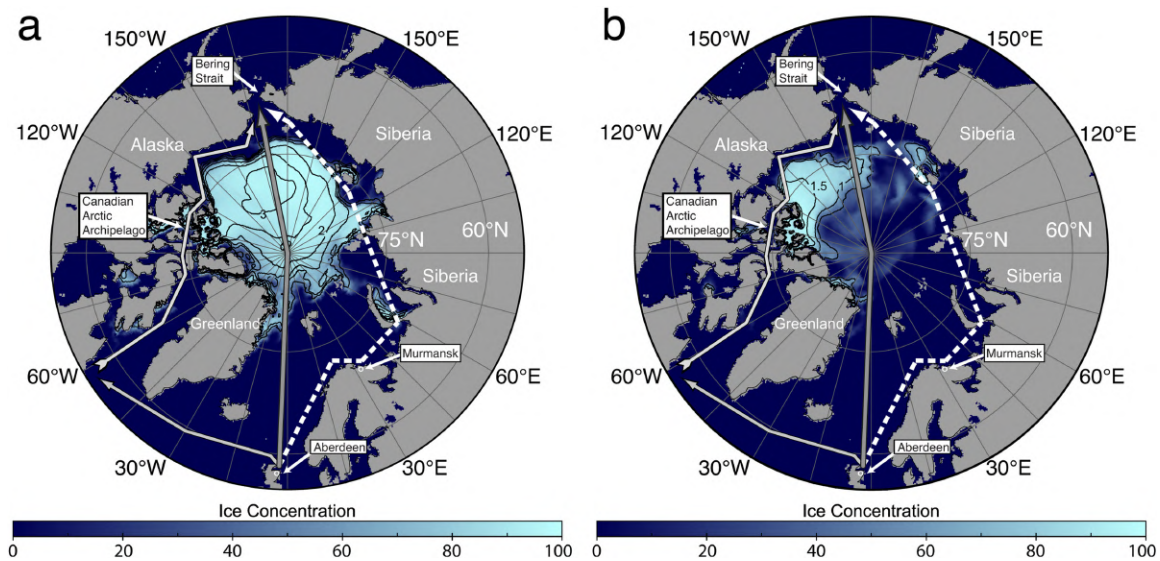


Figure 1.1: Sea ice concentration (% , shades of blue) and thickness (labeled contours) during the navigation period (June–October). Model 2010–2019 (a) and 2030–2039 (b)

Some Arctic shipping routes as of today and projections over sea ice concentration are shown in the Figure 1.1 [2]. Two different models for projected averaged summer sea ice conditions are shown. Model a shows the projection made for the summer sea ice conditions in 2010–2019 while model b shows it for 2030–2039. The Arctic shipping routes shown schematically are : the Northern Sea Route (dashed arrow), the North Pole Route (dark-gray arrow) and the Northwest Passage and Arctic Bridge (light-gray arrow).

As the operation in Arctic for vessels to becomes likely, popularity of polar tourism is increasing day by day. Although the vast majority of the ships entering these waters are still fishing vessels, polar tourism attracts tourists in last decade more than ever. Bearing this demand in mind together with increasing accessibility to these routes, it is predicted cruise ships will be seen more in these areas. Although this is an exciting development for the maritime and tourism sectors, it also brings uncertainties in terms of security.

Apart from commercial and civil developments, navies have also taken their places in this race knowing that presence in Arctic regions will increasingly be a criterion for power balance. Countries that are currently continuing their missions in these waters, especially Russia, have been continuing to strengthen their navy for this purpose. Unlike them, coast-guard vessels mostly had taken the burden of polar missions for the US Navy until recently.

The US Navy, which has been conducting studies in this field for a while to strengthen its operational profile, has recently submitted a study to the American congress evaluating DDG 51 (Arleigh Burke class destroyers) type warships in their inventory for use in this field [3]. Based on this, an undergoing procurement program has been in progress in order to increase the number of this class in their inventory.

Today, trans-Arctic journeys still require an icebreaker accompaniments for vessels with conventional bow shape including aforementioned cruise liners and destroyers. However, the forecasts based on the simulations have shown that unaccompanied navigation in the Arctic regions in summer may be likely as early as the 2030s and is inevitable after the 2050s [2]. This accessiblensness implies that new navigable waters will be gained and this brings along significant opportunities for vessels with conventional bow shape to operate in. Understanding the sea ice interaction of those ships are necessary to optimize their design and operational conditions.

This hull - sea ice interaction for typical icebreaker shaped vessels are quite well understood, knowing the fact that they have been in use for a long while and studied well. Depending on their hull shape characteristics, there exist different approaches in order to predict the hull-sea ice interaction resultants. However, all these emergent developments results in need for comprehensive understanding of sea ice interactions for non-typical ice breaking ships as well.

Emerging developments in new technologies make using different tools and approaches possible for such investigations. In addition to experimental measurements and numerical methods, visual assessment methods are becoming another useful approach due to increase in computational powers, storage options, recording quality and the affordability of those devices.

1.1 Typical and non-typical ice-breaking ships

Appearance of the ice capable ships is widely accepted to has its origins in 19th century. Those ships were in use in Hudson River in the US and in the Elbe River in Germany

as well as they were followed by the ones used in St. Petersburg harbour [4]. Owing to continuous developments in shipbuilding industry, icebreakers in the modern sense were developed beginning with second quarter of the 20th century.



Figure 1.2: A polar class icebreaker Kapitan Khlebnikov as it moves across the sea ice [5]

As it is the case with any other special purpose vessels, ice capable vessels are expected to meet the certain criteria including admissible performance, well adjusted hull design and sufficient machinery power. For an icebreaker to satisfy them, it is necessary for designers to understand the environment that an icebreaker is expected to operate in. This being the case, design considerations for icebreakers are based upon understanding the way ice is acting along the hull.

Being able to refer that an icebreaker behaves well in ice condition is contingent upon manoeuvrability and favorable ice breaking performance of this vessel. Correspondingly, a good ice breaking performance requires low resistance and highly efficient propulsion characteristics. In order to evaluate the ice breaking ability of icebreakers, level ice and brush ice conditions are used rather than considering severe ice conditions like ice ridges or multi-year ices. Speed that icebreaker can perform ice breaking operation continually and at definite ice thickness is then determines the performance of icebreakers. Whereas this

performance for ice ridges and multi-year ice is designated by to what extent icebreaker can penetrate to them.

Due to the fact that the focus of the study is to analyse the broken ice floes during ice-breaking process and to establish a correlation between floe characteristics and level ice resistance in the bow region, level ice resistance related design aspects will be discussed from this point on.

In order to understand different hull shapes and the underlying justifications, ice resistance concept should be understood well. Within this context, ice resistance is indicative of the time average of all longitudinal forces acting on the hull which are based upon different origins. Those origins are listed below in their generally accepted form [6]:

- Breaking forces
- Submergence forces
- Sliding forces

The breaking forces result from the very first structure ice interaction which are essentially crushing and bending the ice. Breaking forces' contribution to the level ice resistance at lower speed was evaluated by Riska and was shown that it is about 50 percent [6]. Moreover, generalized overall contribution of the ice breaking component to the level ice resistance can go up to 80 percent, showed Poznyak and Ionov [7].

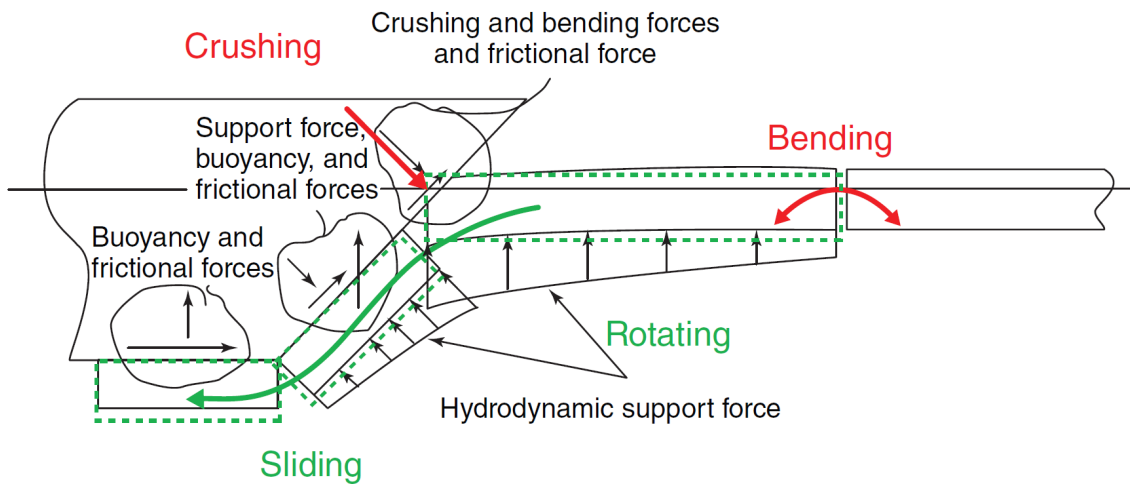


Figure 1.3: The forces present when a ship is proceeding in ice, Riska, The Encyclopedia of Maritime and Offshore Engineering, 2017 [8]

The ice breaking mechanism occurring as the ship moves across in the level ice is represented above in Figure 1.3.

As the ship moves across the level ice, broken ice floes are pushed down by the ice sheet being in the process of breaking. Those broken and submerged ice floes at the bow region then move across the ship hull due to its forward motion. Buoyancy forces act upon those ice floes result in friction between the ice floes and the structure. This motion of the broken ices constitutes the submergence and the sliding forces.

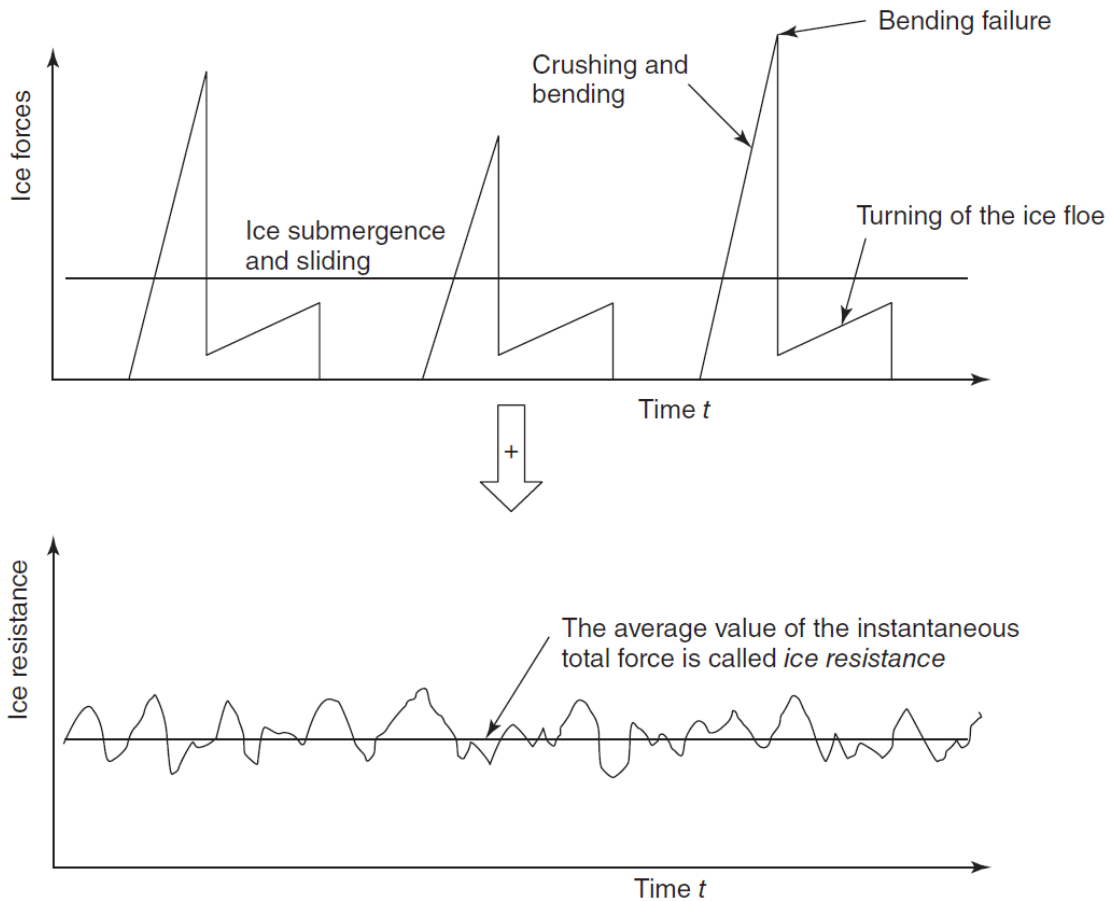


Figure 1.4: The nature of ice resistance as an average longitudinal force, Riska, Design of ice breaking ships [4]

Figure 1.4 above represents the ice breaking resistance act on a ship.

Hull design In order to minimize the ice resistance aforementioned above and to obtain the desired maneuverability, hull shape of the icebreaker has to be designed accordingly. Keeping the ice resistance at optimal range is possible when bow shape and beam of the vessel are designed ideally. Within this context, stem angle ϕ and the beam B are appear as most important parameters.

For typical icebreakers, one of the most differential feature is the stem angle and that is often desired to keep in between 20° and 25° . In other saying, stem angle for a typical icebreaker is commonly kept small as possible as well as is the case with flare angles. The reason for desired stem angle to be small is that to increase the bending contribution rather

than the crushing contribution in the ice breaking process. Wide range of researches have been done which substantiate to the accuracy of this argument. Reduction in the stem angle from 82° to 20° degree decreases the ice resistance by approximately 60 percent, showed Johansson and Mäkinen Johansson [9].

As for non-typical icebreakers those have conventional bow shapes, hull angles' design have different bases. Due to the reason that such bow shapes are mostly designed for open water, their hull-level ice interactions are also different than typical ice breaker vessels. Non-typical ice breakers commonly described to have high stem angles as well as to have small waterline angles. Moreover, waterline angles tend to be kept smaller while flare angles to be kept higher by designers within last couple of decades [10].

These differences in hull angles show their effects on the ice breaking mechanism when the structure and level ice interact. Due to the high stem angle, it is expected for non-typical icebreakers to experience crushing or buckling rather than bending failure of the level ice sheet at the contact point. That being the case, predominance of crushing or buckling failure of the ice along the ship hull is dependent on the normal angles highly. In general, normal angles tend to be on the decline beginning from bow to until about 75 percent of the beam while they tend to increase over again until mid-ship. Bending failures may become superior to crushing and to buckling when normal angles are reduced adequately. Consequently, sliding forces can be upraised based on the probability of different ice breaking modes to eventuate [11].



(a) Conventional bow shaped vessel [12]



(b) Non conventional bow shaped vesse [13]

Figure 1.5: Visual comparison between conventional and non conventional bow shaped vessels

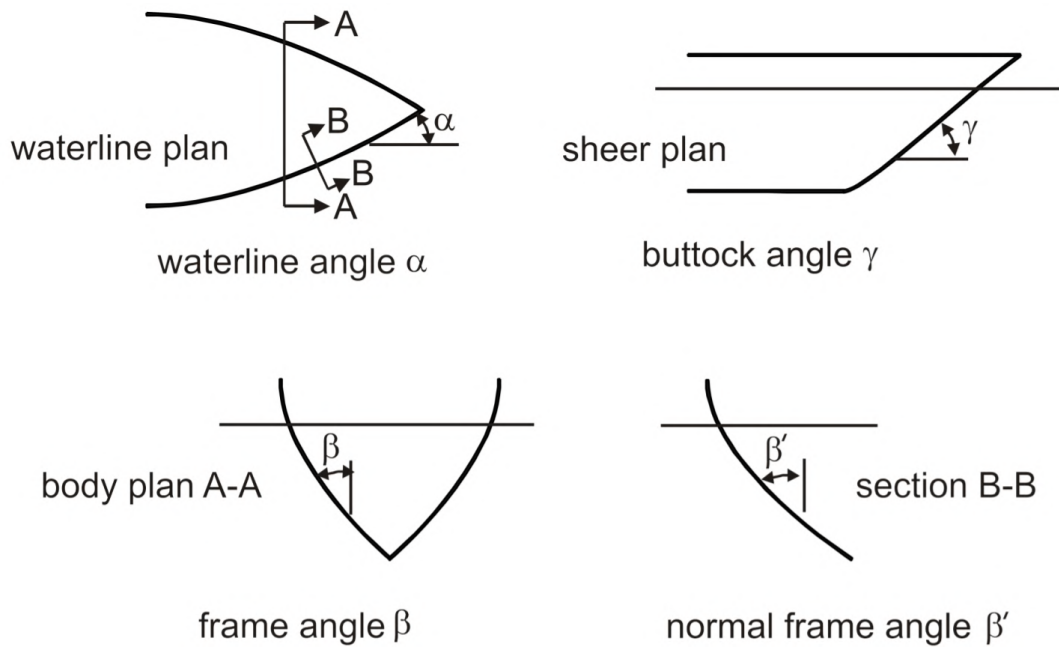


Figure 1.6: Definition of hull angles [14]

Hull angles regarding the bow shape design are shown in Figure 1.6 above where β' is normal frame angle at upper ice waterline, α is upper ice waterline angle and γ is buttock angle at upper ice waterline.

1.2 Image analysis in Arctic technology

Concept of the image analysis is very generically to obtain useful information from an image or from sequence of images. Depending on the task, complexity of the tool and thus range of the information extracted can vary from very basic level to high level. Image analysis concept is in fact very much related to the way human being analysis the surroundings. Considering our vision is in fact a raw data, our temporal cortex extracts specific information from these raw images by processing this data continuously such that segmenting, recognizing and tracking the objects are performed at any given time. Perhaps owing to this analogy, adapting and internalizing the image analysis methods easily have become widespread in many different field of applications. Rapidly emerging developments in storage capacities, cloud based systems, data transfer rate, recording quality and drone technology are stimulating the availableness of the technology.

In parallel to the evolvments mentioned above, image analysis have become a powerful tool in arctic technology as well. Especially satellite images have been used for last couple of decades for this purpose. Those researches were made mostly for having broad knowledge on the sea ice properties, iceberg detection, trends in sea ice extents, sea ice floes and their properties.

Despite the fact that those studies have different scopes, they all are based on the detectability of the ice floes or of the ice extend as object within the environment they are. In Figure 1.7 below shows the process of an image taken by an unmanned aerial vehicle as part of a mission performed by the Northern Research Institute [15]. Analysing such images, researchers aimed to achieve floe size distribution for the benefit of Arctic offshore operations.

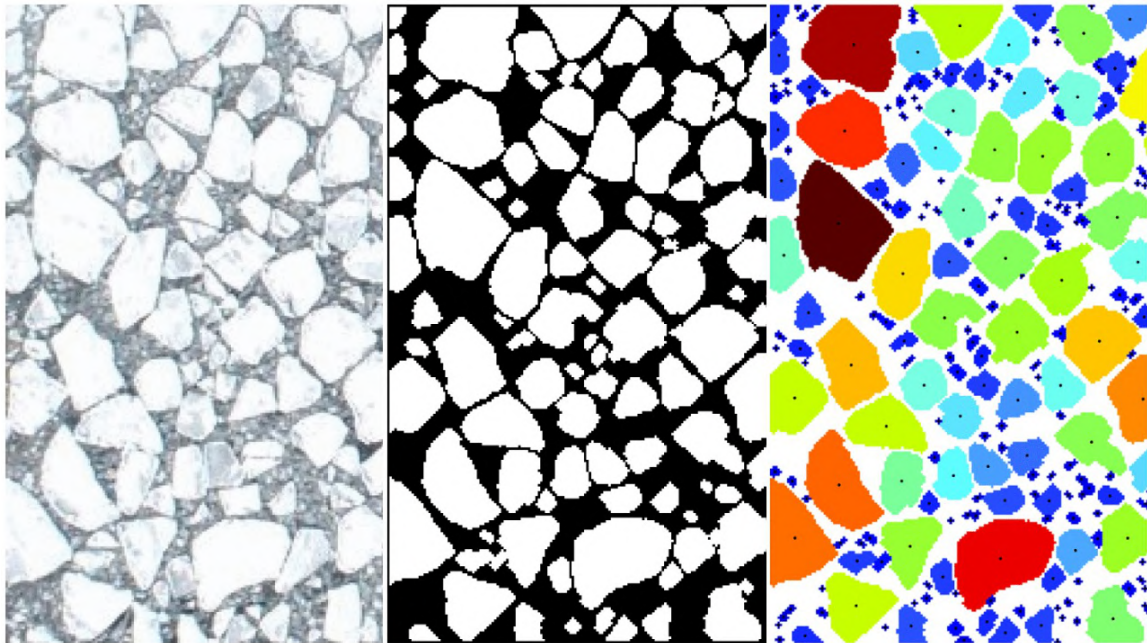
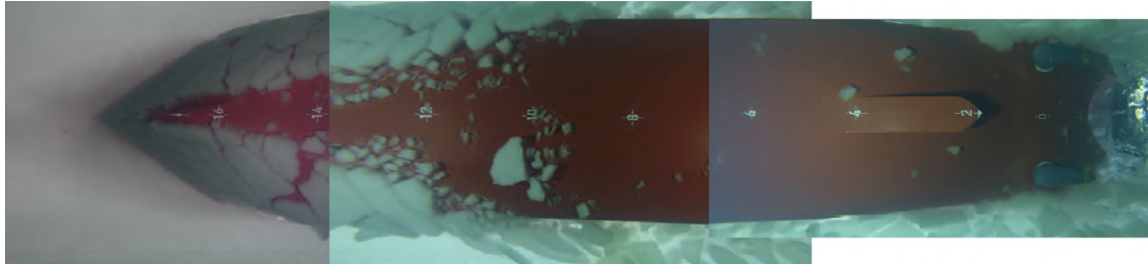


Figure 1.7: Evaluation of an image taken by an UAV and used for sea ice floe properties [15]

In addition to those aerial recording based researches aforementioned, underwater recordings based studies also have potential to contribute in Arctic technologies. For offshore and marine structures in ice, many of phenomena related to relations between ice and structure still remain mystery. Current and future studies in this manner may shed the light on indetermined aspects from structural, design, ice resistance and ice floe characteristics point of views.

Within this context, a study has been done by Myland and included in her doctoral dissertation regarding the experimental and theoretical investigations on the ship resistance in level ice [16]. For this purpose, semi-automated image analysis scripts were developed in order to evaluate underwater images of series of ice model tests. As a result of this, formation and distribution of the ice floes and their influences on the total resistance in ice were analyzed by Myland [16].



(a) Stitched underwater image



(b) Analyzed image

Figure 1.8: Stitched underwater images (on top) and analyzed image with identified ice floes (on bottom) [16]

In Figure 1.8 above, snapshots taken from underwater cameras stitched together on top as well as identified and labelled ice floes on bottom are shown.

1.3 Ice model tests in Arctic technology

In marine and offshore technology, model tests have great importance both for design and for development processes. In this context, ice model tests are performed in order to shed light on ice going vessels' design optimization and operational profiles and are vital. Moreover, the feasibility of some unconventional methods which can lead some outstanding performance results would not be proven unless ice model tests are performed.

Ice model tests are important not only for icebreakers but also for ice going merchant ships, floating structures and fixed platforms. Depending on the model to be tested, test environment and instrumentation are also prepared accordingly. In ice tests, models are generally subjected to first and multi-year level ice, brash ice condition, ice ridges, ice floes and rubble, first and multi-year ridges. Resulting from such tests, wide range of information related to maneuvering characteristics in ice, power predictions, ice breaking performance, ice load on the structure can be achieved.

In order to conduct the ice model tests, ice model basins need to be equipped differently from usual towing tanks. One of these purpose built and equipped facilities contains within Hamburgische Schiffbau Versuchsanstalt (HSVA) in Hamburg and ice researches are carried out at this facility.

Within the facility, an air forced cooling system reduces the temperature inside the tank to about $-20^{\circ}C$ and can reach $2\text{ mm}/h$ freezing rate. Mechanical properties of the ice are adjusted depending on the application and based on the patented techniques developed by HSVA.

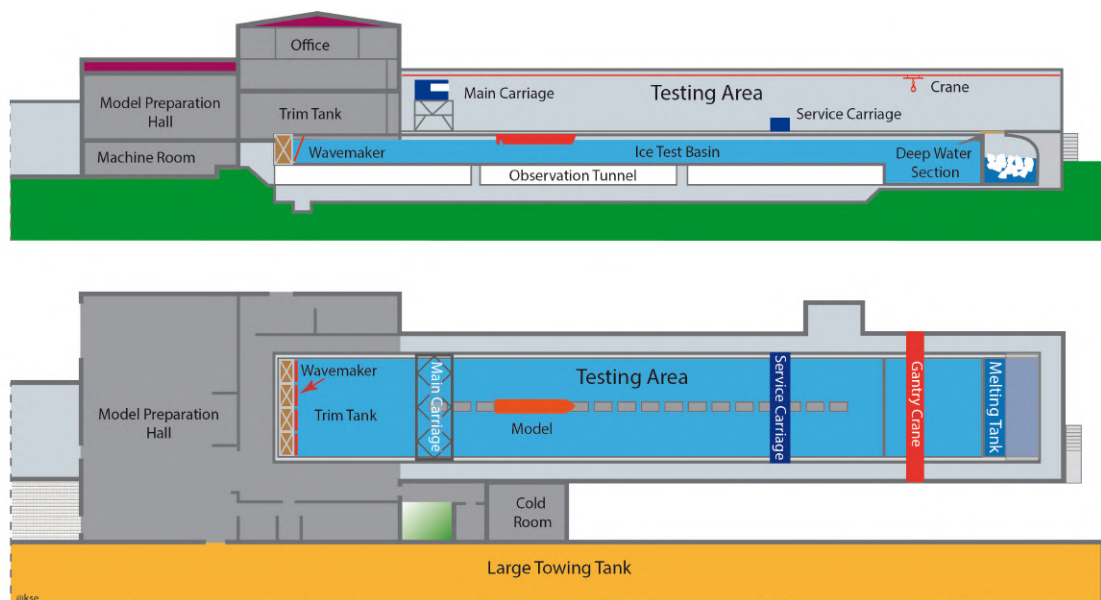


Figure 1.9: HSVA's large ice model basin [17]

Figure 1.9 above shows the HSVA's large ice model basin from different sections. Characteristics dimensions of the facility are 78 meters length, 10 meters width and 2.5 meters

depth including a deep water section at the end which has 12 meters length and 5 meters depth. Additionally, shallow or inland water conditions can be simulated adjusting the shallow bottom covering [17].

Within the ice facility at HSVA, type of the researches commonly made include [18]:

- Level ice and brash ice tests
- Towed propulsion tests
- Fixed mode tests
- Manoeuvring and free running propulsion tests
- Moored floating structures
- Dynamic positioning

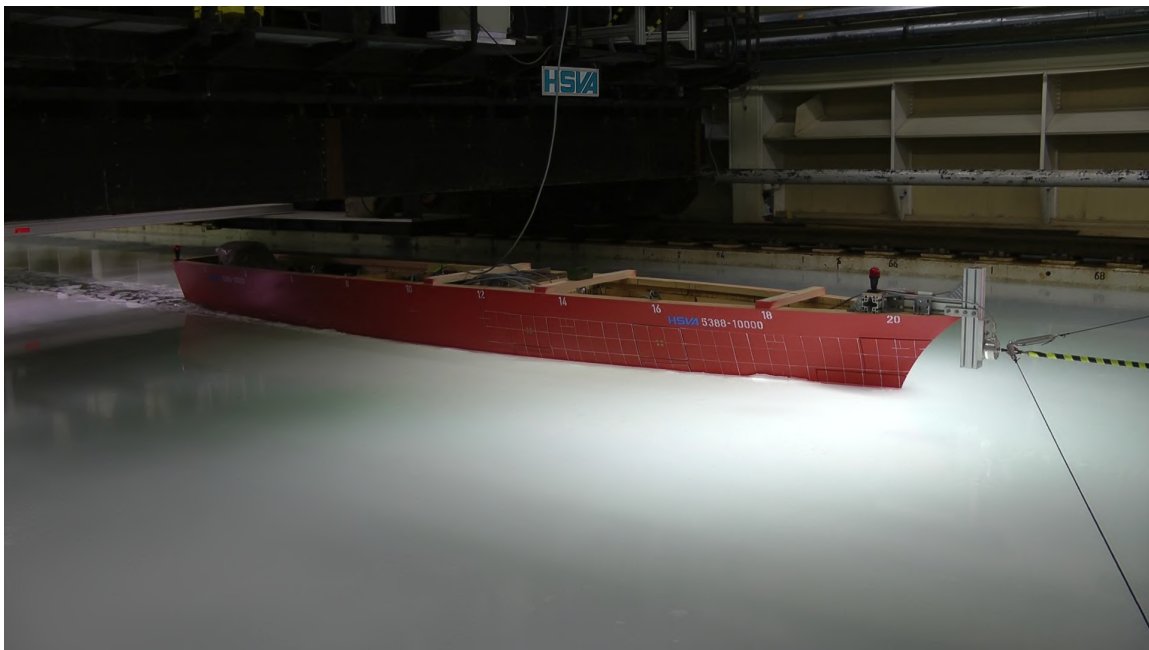


Figure 1.10: Level ice model test at HSVA

1.4 The aim of the study

The main aim of this thesis is to enhance the available knowledge of non-typical icebreaker ship and level ice interactions, by means of determining the ice floe characteristics resulting from this particular ship model and level ice interactions. These determinations are performed introducing a visual observation methodology which is adapting aforementioned image analysis methods to this specific research topic and material. Furthermore, key findings resulting from visual observations are aimed to be compared with experimental measurements in order to evaluate the existence of relation between each other.

Chapter 2

METHODOLOGY

One of the key points for the research to produce desired results is to process the input data with minimum error and to reach meaningful information with minimum effort. In this way, efficiency of the method and the reliability and the accuracy of the interpretations regarding the results can be proclaimed. Hereby, methods and tools presented were studied just in specific to the given research material.

In this context, the methods and tools will be presented in this section which were adopted to attempt to reach these outcomes. Beginning with experimental setup and input conditions provided by HSVA, each factor which can effect the research outcomes will be shown explicitly.

2.1 Experimental setup and input variables

Forming the basis for research is in strict relation with the adjustments within the test environment as well as with the preparation of the experimental setup. These preparatory processes carried out by HSVA will be introduced in this section to the extent relevant to this study. The preparation of the experimental setup can be viewed mainly under these three headings:

- Model construction
- Model instrumentation
- Specifying the test parameters

In order to conduct the experimental investigations, a ship model has been manufactured at HSVA's workshop. Following that this model manufactured for the research was instrumented in parallel with the aim of the research.

2.1.1 Ship model presented for the research

This ship model for the experimental investigations is decided to be based on the model DTMB 5415. Concept of this model series is pertain to preliminary design of a Navy surface combatant. These navy ships are designed to be multimission destroyers and the precursor design of the DDG 51 Arleigh Burke destroyer class which is operated by United States Navy is also considers this reference geometry.

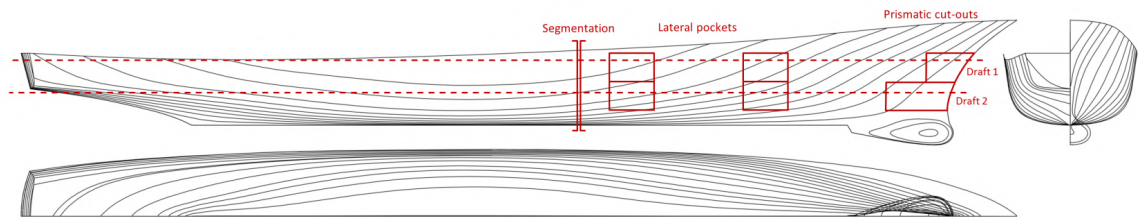


Figure 2.1: Hull lines of the reference ship DTMB 5415 [19]

The ship model geometry as well as the hull lines are shown in Figure 2.1. Remembering the characteristics of typical icebreakers and conventional bow shaped vessels presented earlier in the study, one can confirm the differences in stem, buttock and waterline angles with visual check.

Since the numerical values are measured and studied based on model scale, similitude law of Froude has to be applied in order to achieve the full scale ship values. This scaling factor to be applied between the test model and the full scale ship is $\lambda = 22$. The main characteristics belonging to the reference ship DTMB 5415 are shown in Table 2.1 below.

Main characteristics of the reference ship			
L_{PP} [m]	142.00	Displacement [m^3]	8424
L_{WL} [m]	142.18	WSA [m^2]	2973
B_{WL} [m]	19.06	C_B [—]	0.507
T_{design} [m]	6.15	Propulsion [—]	2 x FP

Table 2.1: DTMB 5415 ship characteristics

Herewith, the wooden model was manufactured and instrumented within the mechanical workshop in the company. Since high precision and accuracy are required in model geometry, computer aided manufacturing methods are also included in manufacturing processes in addition to traditional methods.

Instrumentation of the model has great importance and based on the objective of the measurements, the model had to be modified accordingly. It was known that the geometry of the reference ship would require the model to be instrumented in the way to perform multi-purpose measurements. High stem angle and relatively small waterline angles that model introduces different failure modes as model moves across in level ice. In order to be able to measure force components resulting from such ice breaking process, multi component load cells decided to use on the model.

Later on prismatic cut outs at the stem and lateral pockets at remaining bow region were created. By doing so, crushing loads at the stem and breaking loads at laterals can be measured. Creation of prismatic cut-out and lateral pockets was repeated in the way that measurements can be performed for two different draught values. In addition to these, model was segmented into two main parts which are bow region and the remaining part of the model. A six component scale was placed in between segmented sections in order to measure the loads between them. Lastly, one uni-axial load cell was installed at the bow which connects the model to the towing carriage and measures the total pulling force. These lateral pockets, prismatic cutouts can be seen in Figure 2.1 and in Figure 2.2.

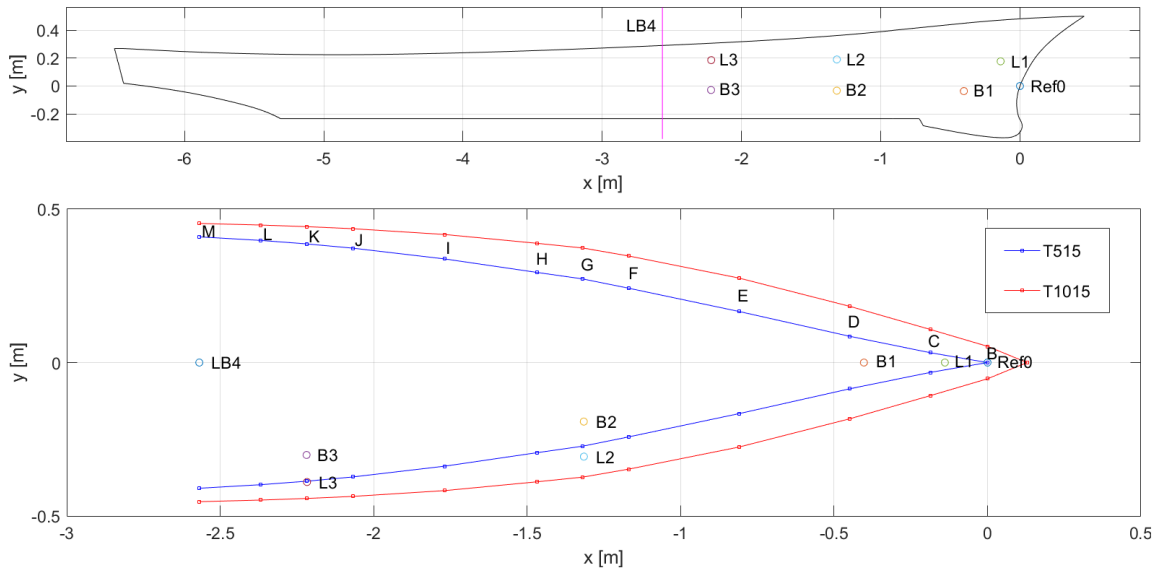


Figure 2.2: Instruments installed along the model [19]

Positioning of the instruments are shown in Figure 2.2 above where $L2$, $B2$, $L3$, $B3$ are lateral pockets, $B1, L1$ are prismatic cut-outs and $LB4$ is segmentation. A real image of the bow section is shown in Figure 2.3 and aforementioned instrumentation can be seen.



Figure 2.3: Side picture of the model at HSVA's workshop

2.1.2 Test parameters

In this section test parameters developed by HSVA and given to the author as input conditions are shared.

Level ice properties Standard procedure was followed in order to produce level ice sheets for tests. Producing level ice sheets processes mainly need to meet the target properties which are ice thickness and flexural strength of the ice. These target properties were checked on a regular basis during the level ice sheet formation in the large ice model basin. This check is consisted of a bending and compression tests of the ice sheet samples as well as of thickness measurements of the ice sheet samples from taken from different longitudinal sections.

Property	Value	Unit
Flexural strength	750	[kPa]
Density of the ice	860	[kg/m ³]
Hull-ice friction coefficient	0.0716	[–]

Table 2.2: Target values for level ice properties

Draught values to be tested As it was mentioned before tests were decided to be run at two different draught values and instrumentation of the model was done based on this determination. Decision for this was made by HSVA based on this particular ship model to be tested. Having sufficient variation on hull angles and thus making sure that different ice breaking mechanism to be introduces along the model was desired. In addition to this variation in hull angles, beam to draught ratio was decided to be kept same for both draught values.

Draught	Value	Unit
Ballast	5.15	[m]
Loaded	10.15	[m]

Table 2.3: Draught values, in full scale

Ice thickness and model speed values In order to see the influence of the ice thickness on ice breaking performance and observations, a set of level ice thickness and model speed values were determined. These determinations were done by HSVA considering the typical range of values for the model tested type of ship.

Following described preparation processes, test executions could be performed finally. Eventually, three different level ice thickness values were tested for each draught value as well as each speed value is tested for each test run. This also means six different test runs were performed and analyzed in this research. The order of the test runs are defined in the test matrix, Table 2.4.

Draught	Ice thickness	Speed
[<i>m</i>]	[<i>m</i>]	[<i>kts</i>]
5.15	0.55	2-3-4-5
5.15	0.69	2-3-4-5
5.15	0.84	2-3-4-5
10.15	0.55	2-3-4-5
10.15	0.69	2-3-4-5
10.15	0.84	2-3-4-5

Table 2.4: Test matrix, in full scale

Experimental setup was adjusted based on the test matrix presented and experiments were conducted by HSV A accordingly. Following points were considered and ensured by test team.

- Rigidity of the connection between model and towing rod was provided
- The flexural strength, the friction coefficient and the ice density were kept constant for each test run
- Model was towed by the carriage at constant speed

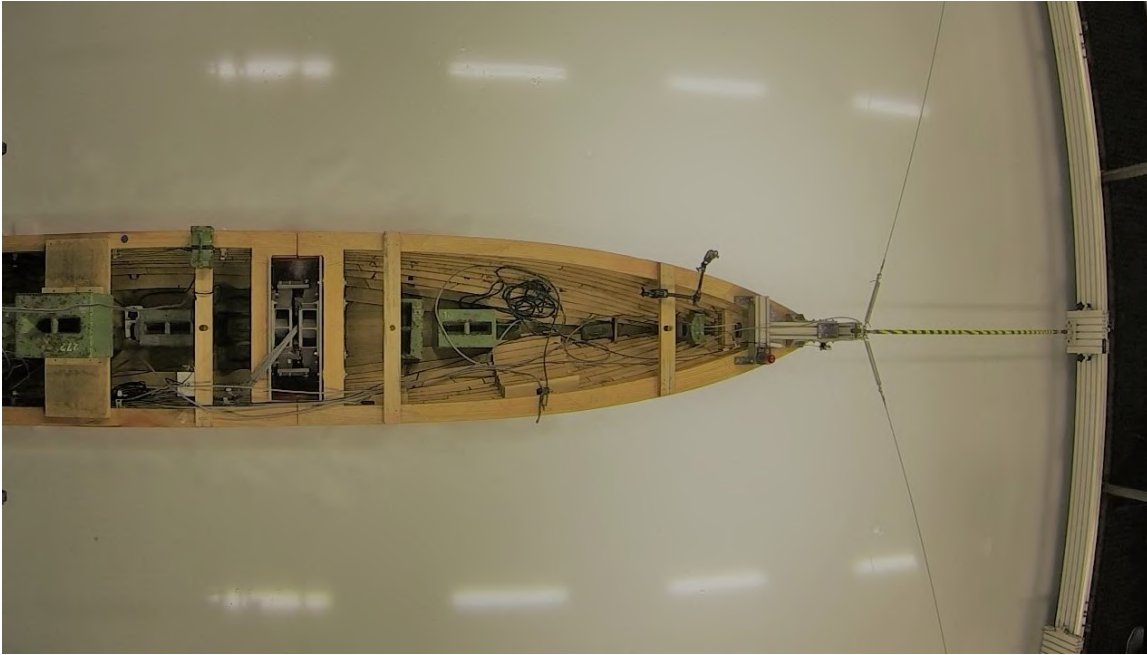


Figure 2.4: Top view of the model as it is towing by the carriage

2.1.3 Recording the test runs

In order to obtain the visual data which is absolute must for image analysis, test runs have to be recorded in the way that recordings meet the required observations. Since for image analysis algorithm to perform the processes successfully depends on the quality of the input data, it is important to record as high quality, clear and stable images as possible.

For this purpose, there are several recording devices placed both under the water and above the water surface. Underwater recording system is consisted of three cameras which are capable of full HD recording and adjustable layout depending on the angle desired. This recording system is mounted on an underwater carriage and this carriage can be controlled by an operator remotely. As model moves forwards along the ice tank, underwater carriage follows the model. Thus, ice breaking process and the motion of the broken ice floes can be recorded thoroughly. These recordings are the basis of the input data used for image analysis.

In following Figure 2.5, some examples to aforementioned various recording angles are given. Two different angles from underwater carriage are shown on the left hand side and

on the right bottom whereas front camera angle from towing carriage is shown on the right top.

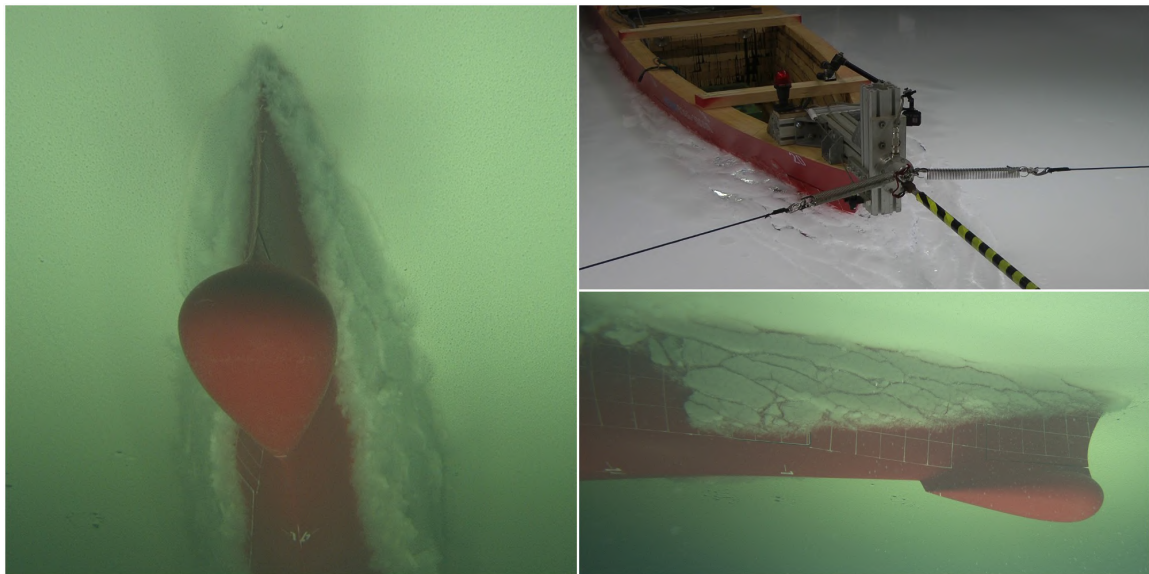


Figure 2.5: Underwater and front camera snapshots of the model

Images taken from side camera view shown in the lower right-hand corner is used in this study.

2.2 Decision making on using the python and the scientific library

Experimental setup given in detail earlier was built by HSVA in the way of providing an opportunity to perform image analysis using the underwater recordings. Although recording the test runs adequately provides the input images for analysis, a sequence of image processing phases have to be executed for achieving useful information. To do this, a software tool has to be used or an algorithm which is customized based on the research material has to be developed.

As it is the case for other engineering needs, many software are available for this purpose. User is obliged to proceed with the one considering to what extend that tool responds to the research need. Within this context, an open source image processing library Scikit-Image

[20], for Python® programming language, is used to built image analysis algorithm in this study. Library found by Stéfan van der Walt and was released in 2009. Since then, it has been written by active community volunteers and can be used free of restrictions. Decision regarding this library to be used is made based on availability of the sources, effectualness of the progress, possibility of interdisciplinary transitions and how wide is the range of the information to possibly obtain.

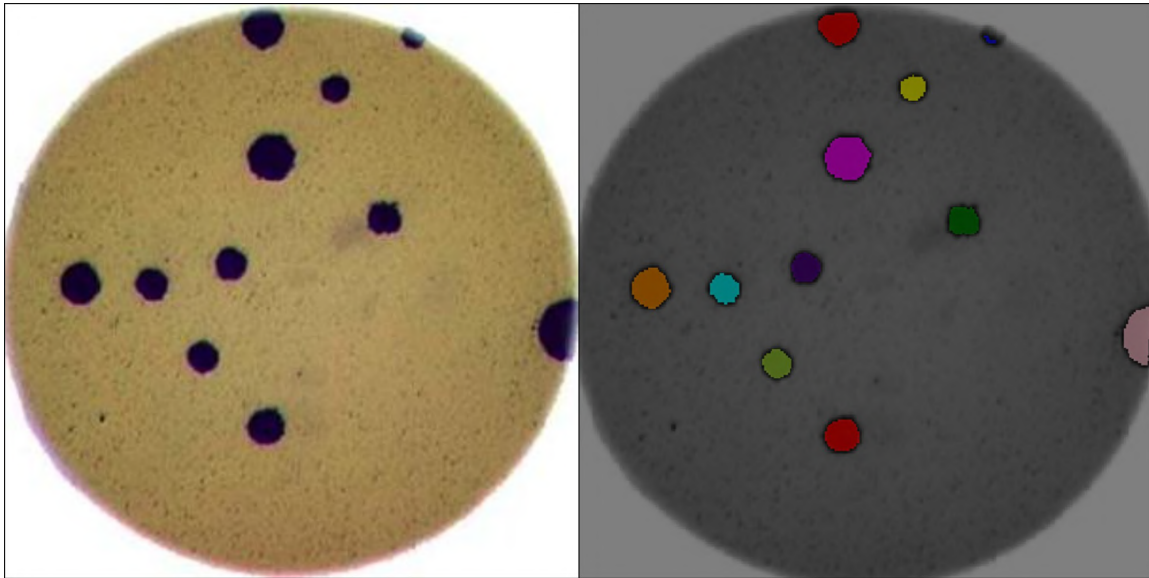


Figure 2.6: Counting bacteria in petri dish using Python [21]

An example scientific work performed using image analysis is shown in Figure 2.6.

2.3 Developing the algorithm and implementation

As a result of the processes themselves being pixel-based, regardless of the content in the images, similar mathematical approaches are applied to analyze the features in the images. Counting the blood cells in a microscopic image and finding sea ice distribution in an image taken from satellite may have differently adopted but common fundamentals. These fundamentals were used in favour of this specific study and steps in the tool development process and the implementation of the method will be described in detail in this section.

Visual information in real world are displayed using 2D pixels in images. Changing properties of these pixels between each other makes demonstrating object and color variations

from real world in images possible. Main variable of a pixel is intensity of the pixel and intensity of a pixel is expressed within a range. This range for most of grayscale images is between 0 - 255. For most color images, red, green and blue channels are used owing to the fact that any color can be built using the combination of these three. Then each channel needs to be defined within 0-255 range. Grayscale images needs a lot fewer storage than color images need. Therefore they are commonly used in image analysis algorithms as well as in this study. Manipulating these intensities of pixels forms basis of most of image processing methods. Figure 2.7 below represents grayscale and RGB color model.

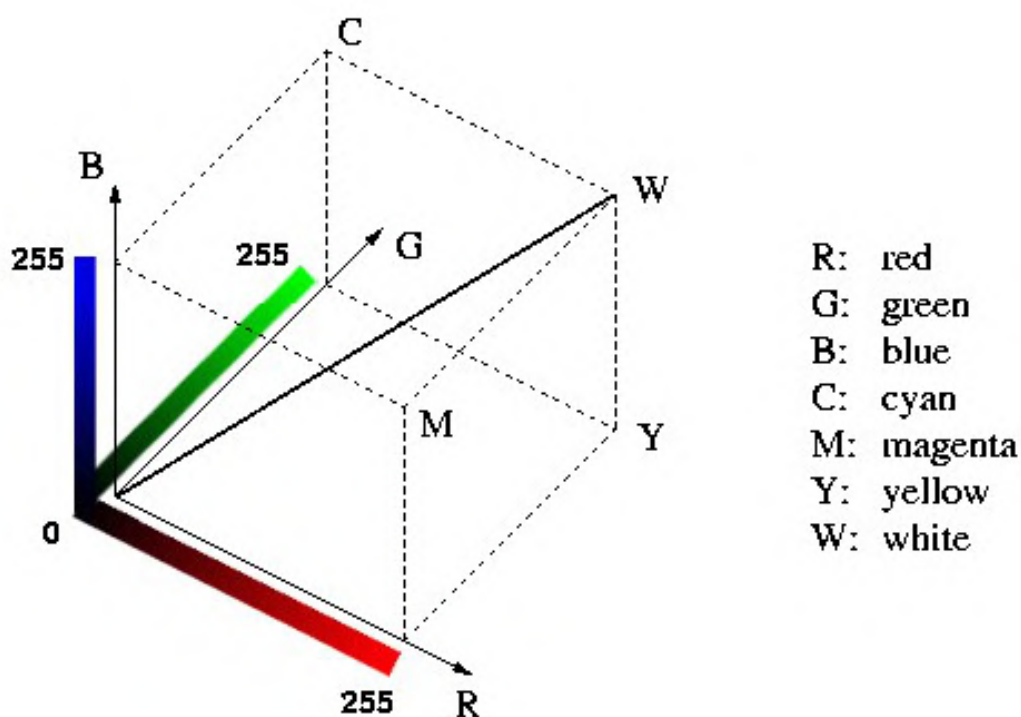


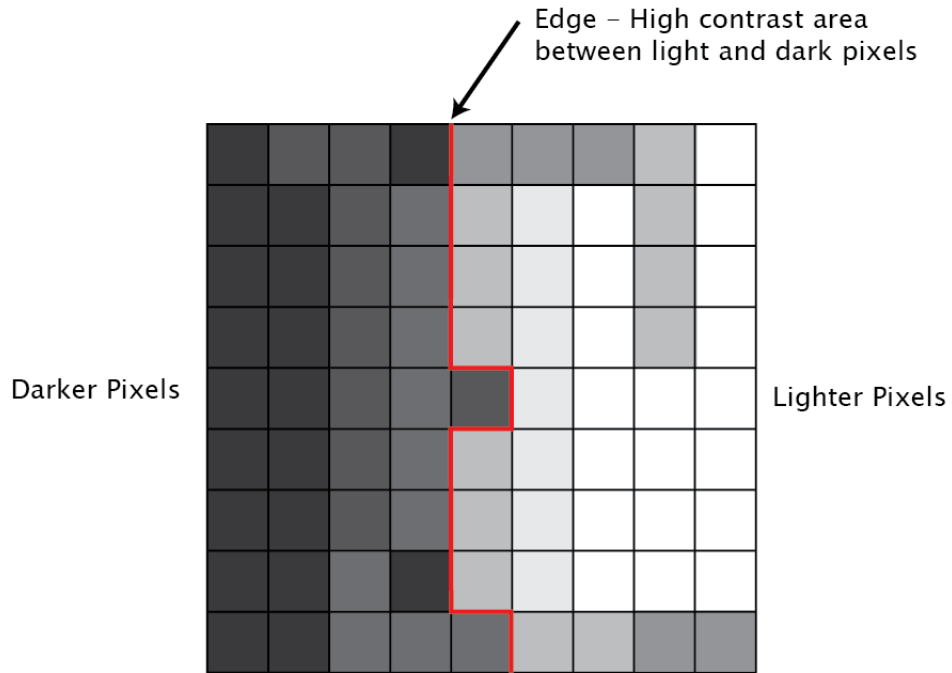
Figure 2.7: Grayscale and RGB channels representation [22]

Since the purpose of this study is to analyse broken ice floes, feature detection based algorithm is built assuming that the each broken ice floe are an individual objects in the input image. This algorithm is consisted of two modules. First module is used as pre-processing step in order to obtain useful information from the image This information coming from pre-processing is then expected to be the basis of the second module which performs feature detection.

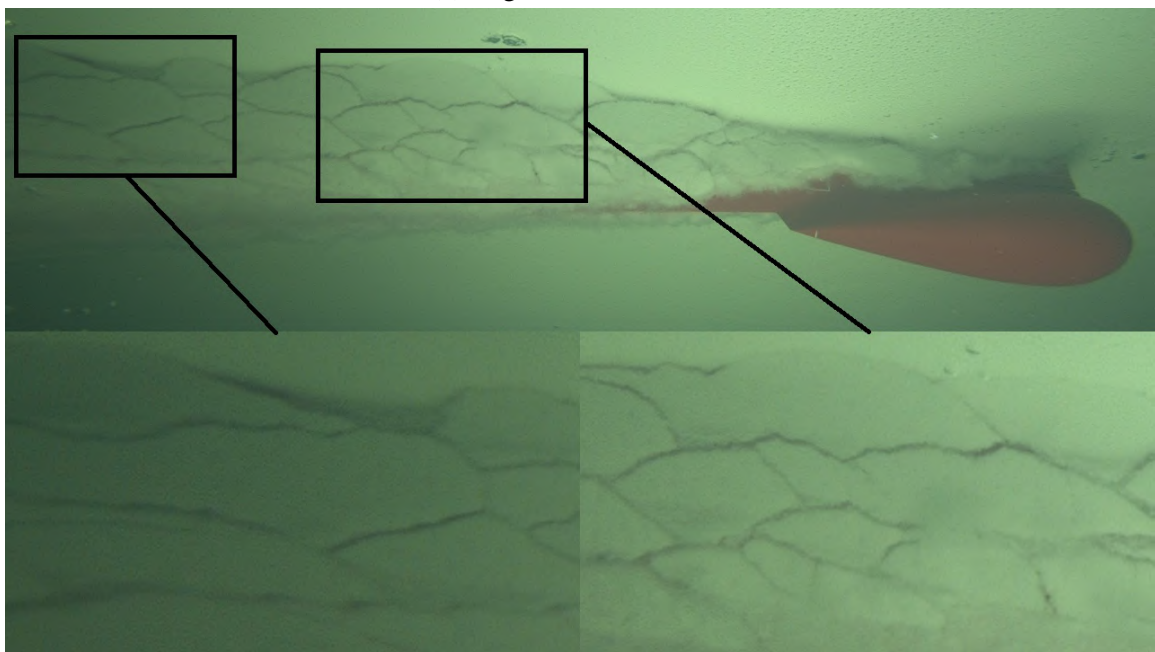
In order to develop the algorithm and to detect broken ice floes in the input image, the

feature that differentiates the broken ice floes from all the other candidate objects in the input image must be determined. To do this, randomly taken snapshots from underwater recordings were examined.

A snapshot taken from underwater recordings is shown as an example in Figure 2.8 (b) below. By looking at the breaking pattern, one can spot the borders between ice floes owing to the color difference between the ice and model hull. That also means high contrast changes are occurred around the neighbor pixels at broken ice floes' borders. The way algorithm defines edges based on this contrast information can be seen in Figure 2.8 (a). Owing to this fact, using edge detection approach makes broken ice floes' detection possible for the given underwater recordings.



(a) Edge definition [23]



(b) The way edges of ice floes look underwater

Figure 2.8: Edge definition and close look on ice floe edges

Following this, the most convenient parameters for the given image are transferred to the second module which contains morphological operations necessary for segmenting the image successfully. Diagrammatic representation of the algorithm including both modules is shown in Figure 2.9, by way of step-by-step approach to solving the task.

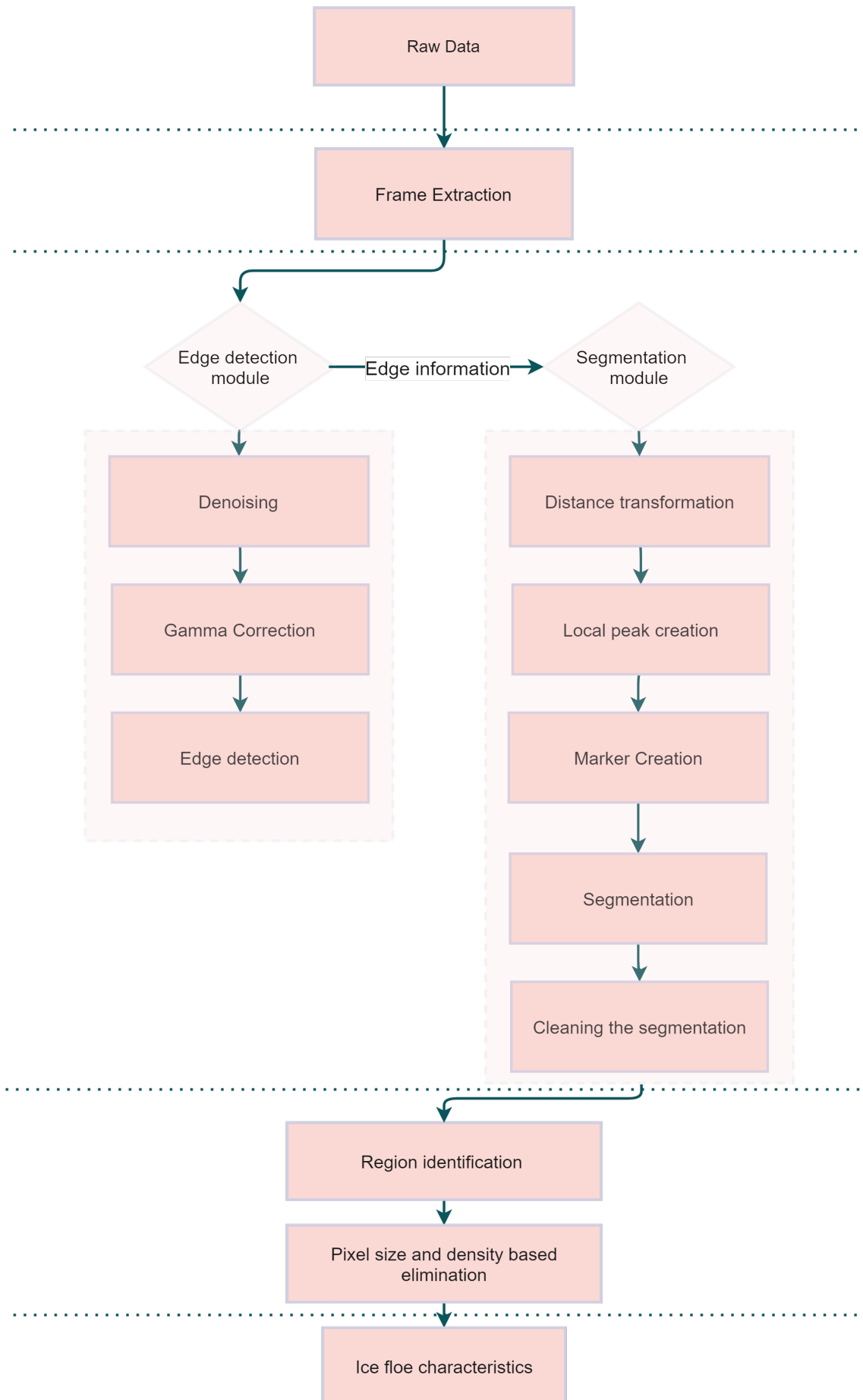


Figure 2.9: Algorithm tree

2.3.1 Image pre-processing

First module in the algorithm is consisted of several operations which basically aims to improve the raw image in order to improve detection of the edges by means of eliminating undesired features.

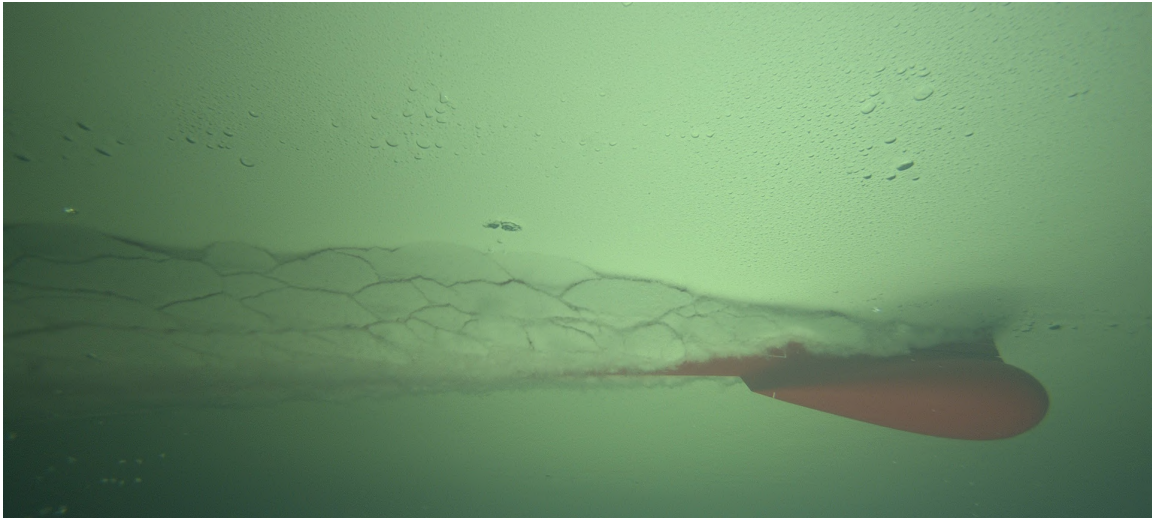
Raw images include many environment related details inherently. These details cause non-smooth transition in pixel densities and thus lead the algorithm to produce highly distorted output images which are impossible to extract any useful information from. It was seen that the raw images extracted from the recordings contain such undesired details due to the air bubbles and to the irregular brightness distribution over the frame. Therefore restoration over image is needed.

To do this, `non-local means denoising` method was implemented using the `restoration` package. This method was found more beneficial than others considering the specific and heterogeneously distributed texture of the images. The method is based on basis of adjusting the pixel values to its neighborhood. This neighborhood is to be defined by the user setting the patch characteristics. Image patch term here defines the subdivided blocks within the images which are used to set the parameters within.

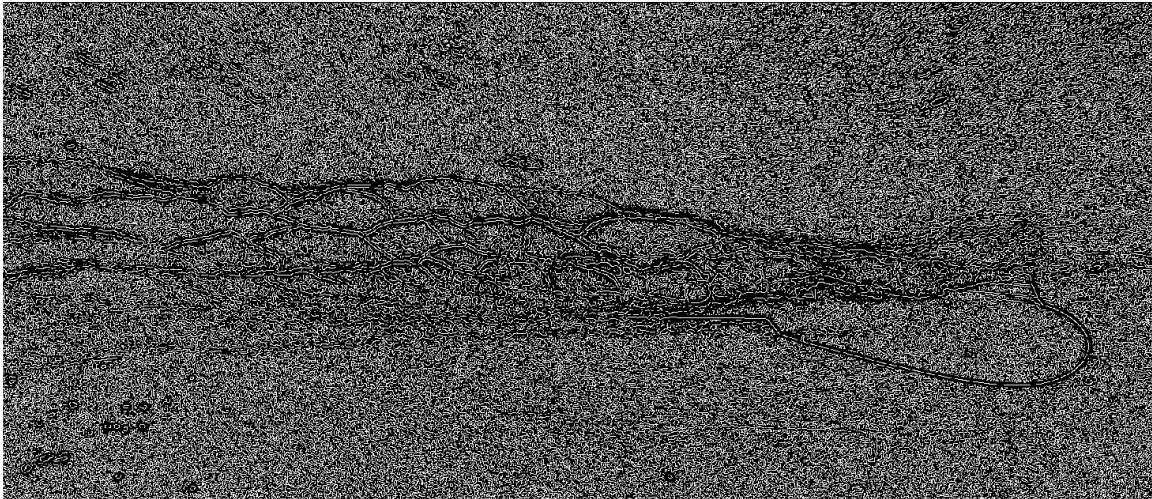
In order to improve contrast in favour of the desired details in the image, power law transform was applied implementing the `adjust-gamma` method given in `exposure` package. Setting the gamma value, user can change the brightness of the output image in the way of that for gamma greater than 1 histogram will shift towards the left and for gamma less than 1 histogram will shift towards the right. This histogram is given for the grayscale image and a shift towards left results in darker pixels while shift towards right results in brighter pixels.

Finally edge detection is applied to previously improved image. Although there are numerous edge detection approaches in use, Canny method given in the `feature` package was seen by trial and error to be more suitable for this study. There user defines standard deviation of the Gaussian filter as well as upper and lower bounds for thresholding.

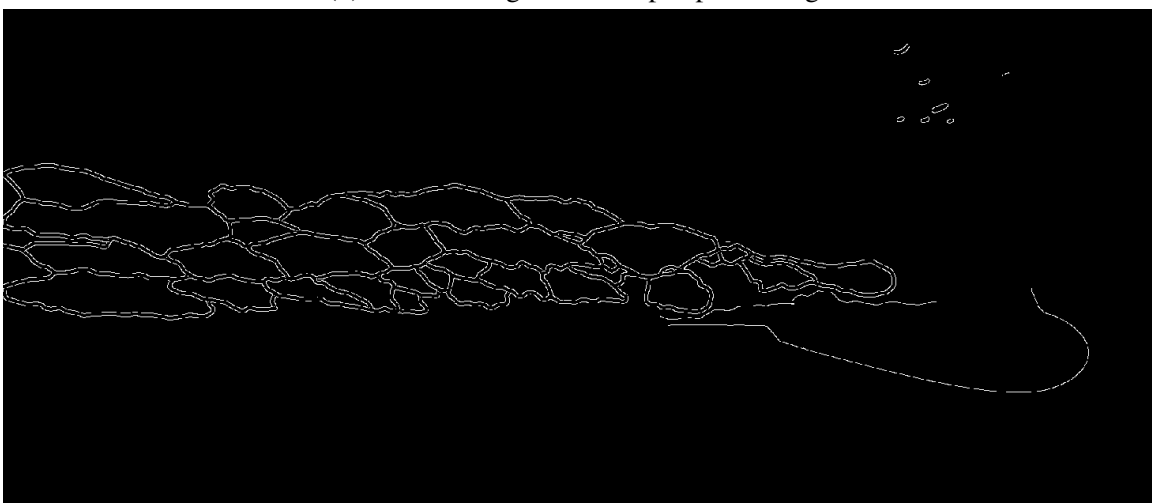
The improvement that aforementioned methods provides as well as the difference between detected edges with and without pre-processing are shown in Figure 2.10.



(a) Input image



(b) Detected edges without pre-processing



(c) Detected edges with pre-processing

Figure 2.10: Input and output images processed in the first module,

Once the most convenient parameters are set, those parameters are then used in second module and thus detected edges form basis for the segmentation.

2.3.2 Image segmentation and morphological operations

Second module in the algorithm focuses on the morphological and shape related non-linear processes. These morphological operations fundamentally prepares the image for the segmentation. These methods have to be chosen depending on what sort of segmentation methodology will be followed. Although numerous methods are available within segmentation module, watershed approach is decided to implement. Robustness of the algorithm to segment the objects in the images was an important criterion when choosing the method. Also boundaries among the ice floes were seemed fitting well with the approach presented. To make sure that method fits well, some other approaches were applied at first phases, however results were not found satisfying. For the underwater images specific to this study, it is seen that the watershed algorithm provided better accuracy as well as the globally segmented image it gives is more favorable.

Watershed approach developed by Luc Vincent and Pierre Soille [24] considers the image as a topographic surface and transforms it into a digitally elevated model. This elevated model is to be described by means of finding the minima based on the pixel intensity and then flooding them out starting from the lowest intensity through the catchment basin. Basic schematic representation of the fundamental approach is shown in Figure 2.11. On the left hand side (a) 2D view of the approach is shown whereas right hand side (b) shows basic 3D approach from topology point of view.

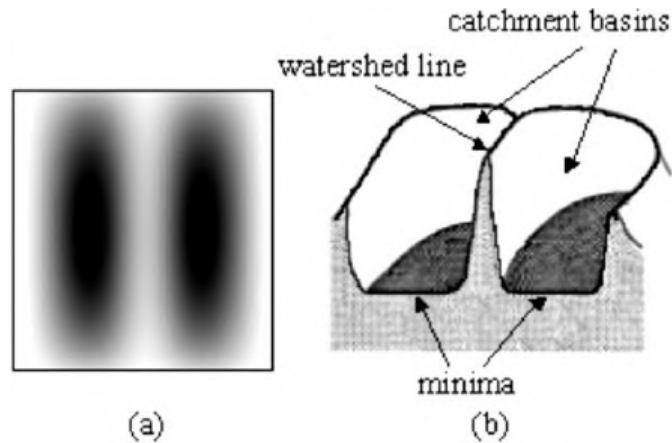


Figure 2.11: Watershed approach in region based segmentation [24]

For segmentation to perform, the topology of the image has to be formed. To do this firstly exact Euclidean distance transform over the image resulting from first module is applied. The distance here means the distance of the detected edges to the closest dark or in other saying background pixels. Later on markers are generated and labelled to be used by watershed segmentation. Figure 2.12 shows the simple representation of the distance transform by means of a binary image assuming that the L is the object in the image (b). Grey level of the image (b) is used to represent the distance values.

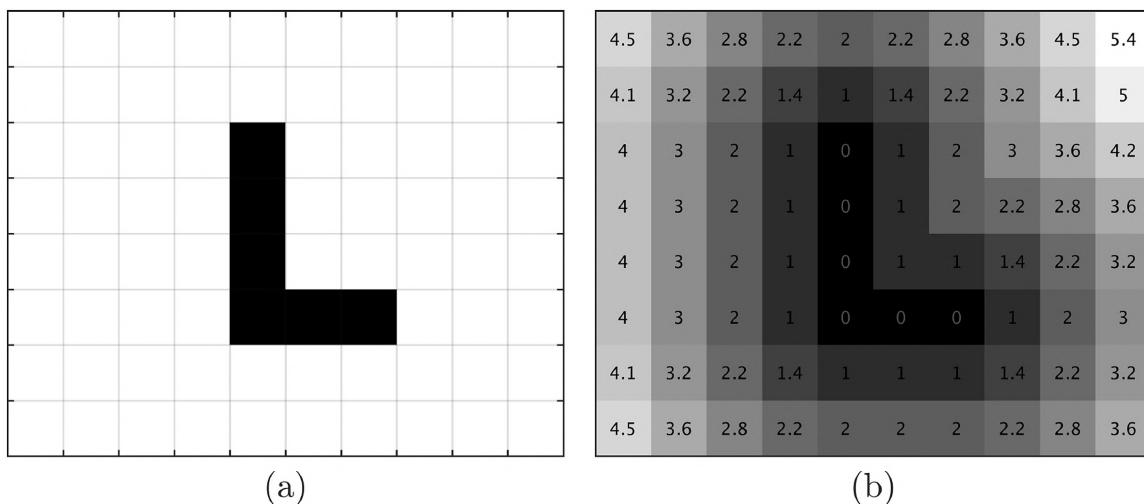
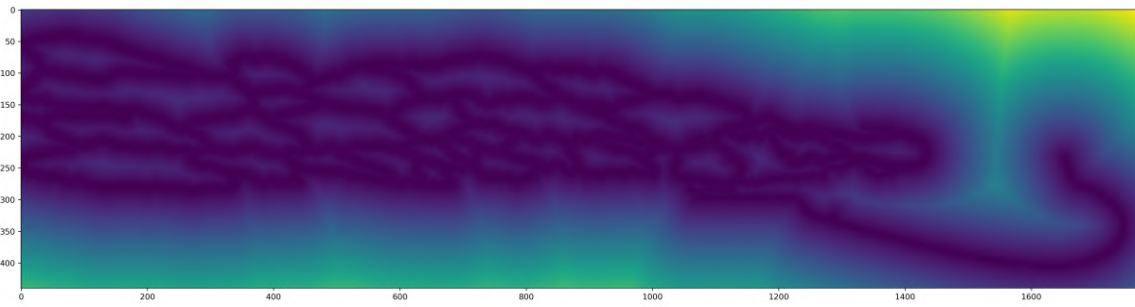


Figure 2.12: An example image with an object in it and its distance function [25]

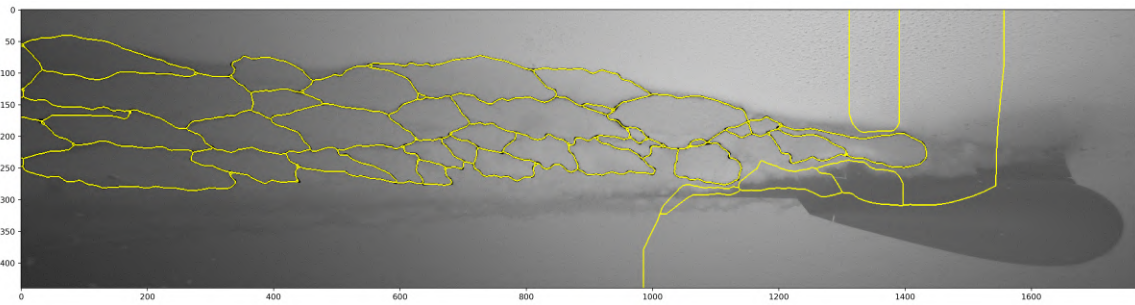
The topography of the the surface elevation was shown in Figure 2.11 principally. First representation of this elevation in real image can be seen in Figure 2.13 (a).

Resulting from second module, evaluation of the segmentation is shown in Figure2.13. Each region formed resulting from segmentation represents a broken ice floe. Once the

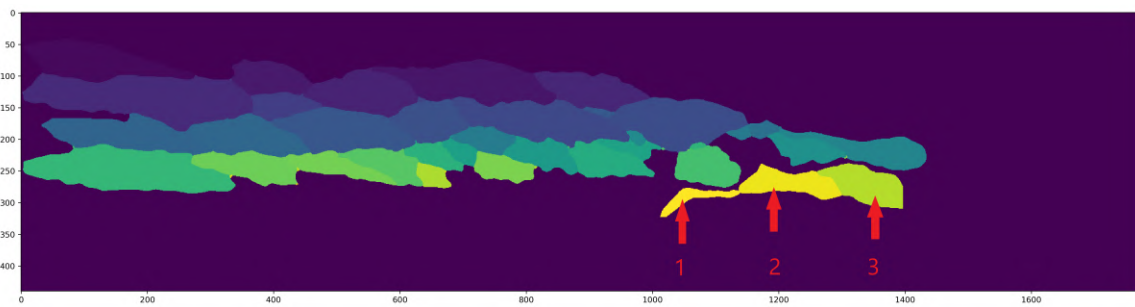
region is enclosed all pixel wise information regarding this region is known and stored. Taking the advantage of this, segmented regions are made overlapped with real images in order to have better visual presentation. Additionally, overlapping images were important to make visual assessment throughout the study and to improve the algorithm accordingly. In some cases, noise may remain in the image or the smoothness of the image can be sacrificed finding a compromise among the parameters in favour of keeping edge details in the image. This may result in over segmented regions in the image. These regions become non representative regions in the end, as they were seen in some of the output images during the study. The image presented in this chapter is one of them and was picked intentionally exemplification. Aforementioned non representative regions resulting from segmentation are highlighted and can be seen in Figure 2.13 (c).



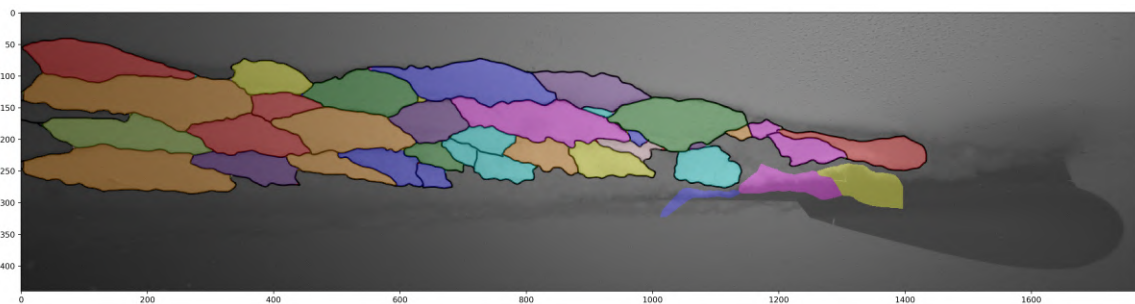
(a) Distance transform applied



(b) Segmentation and resulting regions, overlapped with gray scale image



(c) Segmentation after over-segmented regions removed



(d) Segmented and cleared regions, overlapped with gray scale image

Figure 2.13: Segmentation steps and resulting regions representing broken ice floes

In order to eliminate these undesired regions which in fact do not correspond to any broken ice floe, a logical operation is implemented in the algorithm. Considering the fact that pixel wise information is already known for each region, one can take advantage of their distinctive properties among each others. In this context, it was seen that such regions which do not correspond to any broken ice floe are formed either around bottom of the hull or

around bulb. In these areas model hull is visible and thus the pixel values designated to the this distinct and non representative regions are distinguishably different than the regions corresponding to the broken ice floes.

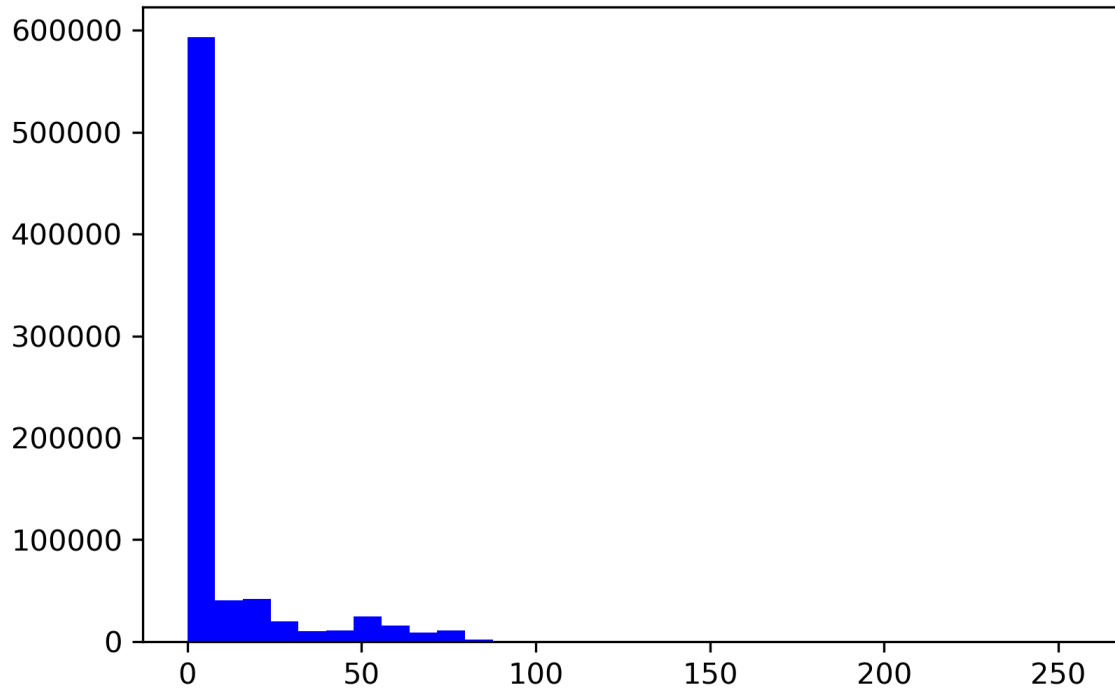


Figure 2.14: Histogram of the segmented grayscale image

In order to see pixel values corresponding to these undesired regions histogram graph of the image shown in Figure 2.14 is used. The horizontal axis of the graph represents the pixel values, while the vertical axis represents the total number of pixels in that particular value. Most frequent pixel value is 0 which are the dark background pixels and greatest values are belong to three regions shown in Figure 2.13 (c).

This elimination is done by checking whether the pixel values of the regions are within the defined pixel value range or not. Principal approach is shown below.

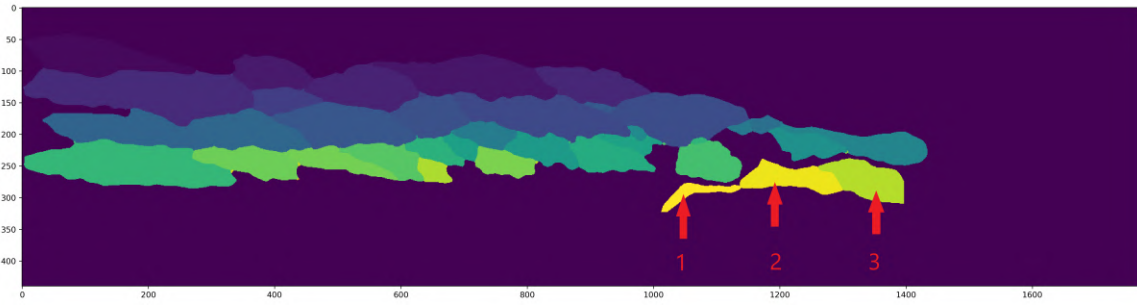
```
1
2 import skimage
3 import numpy as np
4 import matplotlib.pyplot as plt
5
6 for region in regionprops(labelled_segmented):
7     if region.area >= 2000:
```

```
8     # Limits the size of the regions to be considered
9
10    x,y=region.centroid;
11    Centroid_Intensity = segmented[int(x),int(y)];
12
13    if Centroid_Intensity > 0 and Centroid_Intensity <70 :
14        # Only regions within this range of pixel values will be kept
15        .
16        .
17        .
```

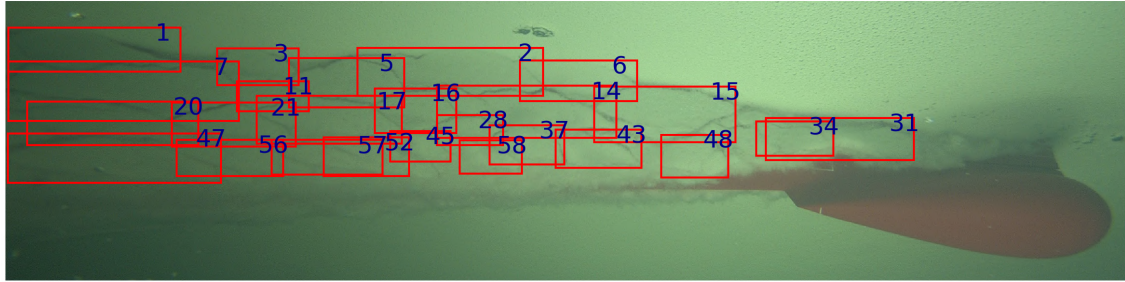
Listing 2.1: Pixel value based elimination of undesired regions after segmentation

In the particular example given above, regions with a pixel intensity of more than 70 and equal to 0 in their centroids are excluded. These upper bounds for pixel intensities were set by trial and error and are usually the far right values on the x axis of the histogram. 0 pixel intensity corresponds to the background pixels and can be used for all cases.

Following this, only regions which correspond to a broken ice floe are kept. In order to show the detected broken ice floes on the original image, a bounding box for each floe with their region identity is added. The final image with these bounding boxes can be seen in Figure 2.15 (b) together with the other image previously shown (a). Having a look on both, removal of the false regions resulting from pixel value based operation can be clearly seen.



(a) Segmented image, before false regions are eliminated



(b) Labelled image, after false regions are eliminated

Figure 2.15: Final output images

2.3.3 User interface built to ease the parameter determination

As in input images are exposed to a process at each step of the algorithm, their information based on pixel values are stored in $n \times m$ matrices corresponding the image size. That means each change made in parameters for each step modifies the image. Detecting edges to be used in second module means actually finding a set of these parameters. A challenge due to these independent changes was that the changes made on independent parameters and their effects on each other could not be seen on the output image simultaneously and instantaneously. In order to fix this issue and to save some time, a simple graphical user interface is implemented. By doing this, resulting changes on output image using different parameter set is made possible to see and control interactively.

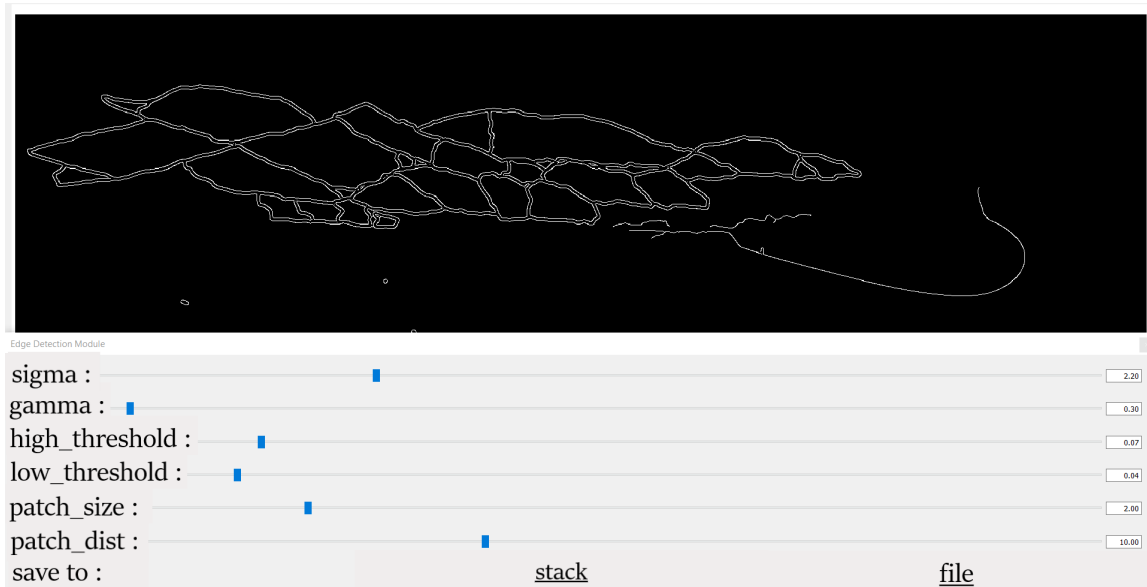


Figure 2.16: User interface for edge detection

This tool made to ease the process is shown In Figure 2.16. Significant parameters can be controlled using the slide bars or entering the values manually. Finally output image can be saved into a user defined directory to be used by second module later on.

2.4 Composing the input data to be analyzed

In order to perform the image analysis, target images to be used in the algorithm have to be obtained priorly. Underwater recordings of the test runs were used for this purpose as source. As it was described earlier in this section, model tests are composed of six test runs. Thus, frames are extracted from each of these six underwater video recordings.

2.4.1 Extraction and classification of the images that can be analyzed

In each video recording, the model was tested at four different speeds. This necessitates to classify the images based on the speed values they belong to in addition to extracting them. To extract frames from video recordings, *scene filter* feature of the VLC Player ® is used. Then, it is determined which speed range these frames belong to in the relevant recording.

In order to make this classification correctly, the starting and ending times of the tested model speeds in the video must be known. Since model was equipped with various instrumentation and test parameters dependent measurements were recorded, time interval data can be used for this purpose. This time interval information recorded is shown in Figure 2.17 for $h = 0.79$ m and $T = 10.15$ m. Although it is stated that the model was tested at four different speeds, since only 2 and 5 *kts* are the subjected to analysis in this study, only data corresponding to these two is presented.

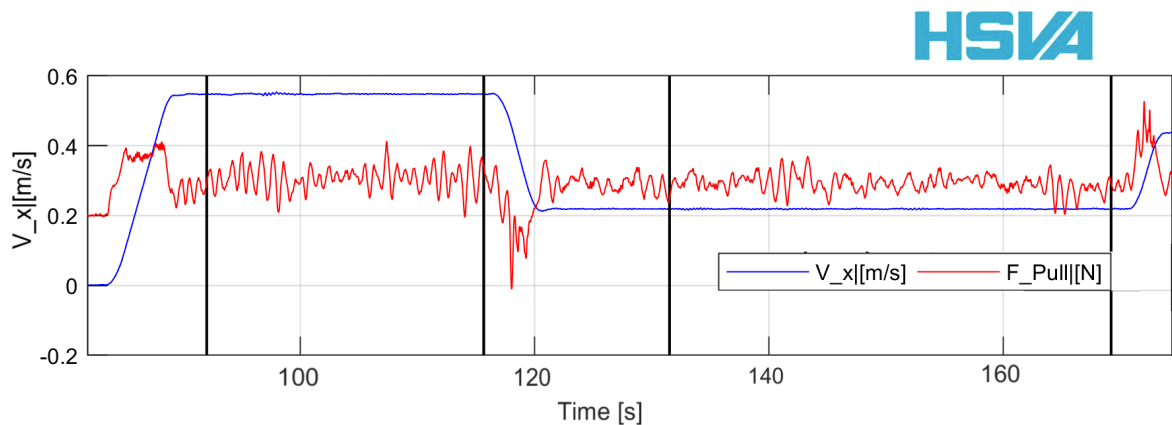


Figure 2.17: Time intervals corresponding to model speeds tested

Blue line in Figure 2.17 shows the model speed whereas red line shows the pulling force applied as model was towed by the carriage.

Once this interval information is known by virtue of measuring instruments on model, a correction between the time seen in the video and seen in the interval data has to be performed. This correction is needed due to fact that video recordings start before the test measurements begin. To find this time lag between them, synchronization signals installed on the model have to be checked. These synchronization signals blink synchronously either when measurement starts or ends. Thus, the time lag between video and *axis* of the measurement data table can be found. In Figure 2.18, the moment synchronization signals activated due to measurement was started is shown for the test run corresponding $h = 0.79$ m and $T = 10.15$ m.

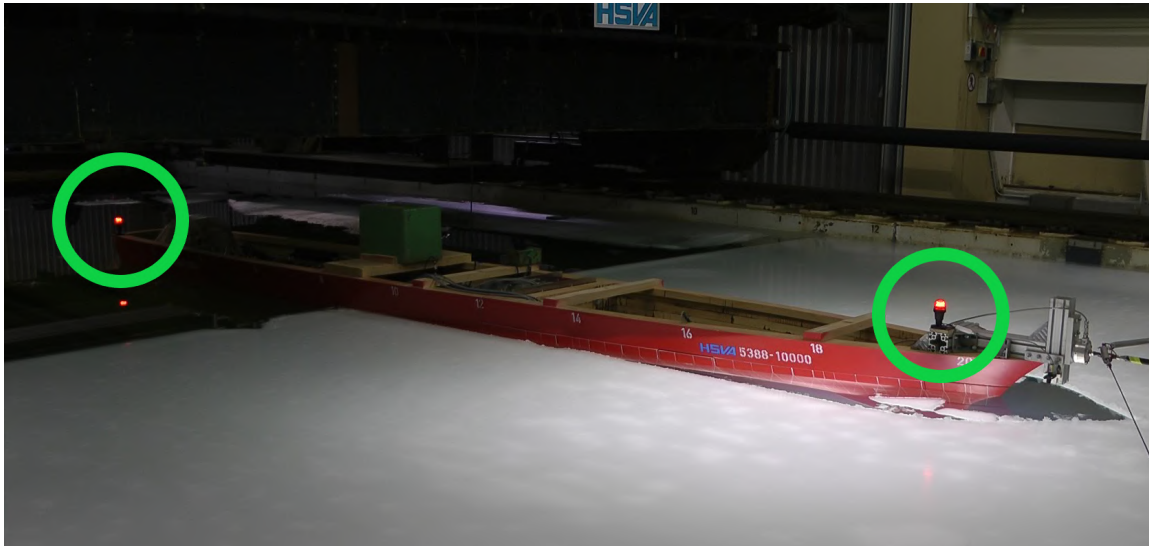


Figure 2.18: Synchronization signals installed on the model

In Figure 2.17, time domain is divided into sub intervals by vertical thick lines. This sub intervals are created to specify the range of measurement to be considered in analysis. Since different model speeds are tested in one test run, model accelerations may affect the accuracy of the measurement and this is avoided restricting the main data intervals.

Once the time seen in the video recording and seen in the interval data are synchronized, moments corresponding to the vertical lines restricting the intervals can be found. Following that, image range to be analysed can be determined by means of matching these moments and the extracted frames.

Resulting from this processes, a table is cited as an example in Table 2.5 which shows the actual data for $h = 0.79$ m and $T = 10.15$ m. Numbers of the frames shown in the table were set specific to each frame automatically by computer depending on the recording ratio defined by user where recording ratio is proportion of the frames desired to extract. For instance, to export 1 in every 5 frames, as is also used in this study, 5 should be entered into the given box in software.

Speed	5 knots		2 knots	
Time interval [s]	85	110	126	163
Frame interval [–]	01111	01416	01616	02061

Table 2.5: Image range that can be analysed within time intervals to be considered

The time intervals shown in the Table 2.5 above have corrected with respect to the time lag calculated and show the intervals in the video recordings corresponding to the intervals represented with black vertical lines in the data table.

2.5 Obtained physical properties from image segmentation

One of the motivational factors behind building purpose specific algorithm is to have wide range of information for detected broken ice floes. As soon as the image is segmented successfully, it is made possible to reach such information range.

Mainly three of these information were printed and stored in a file for each analyzed image. Figure 2.19 below schematically shows them on the segmented image shared as an example before.

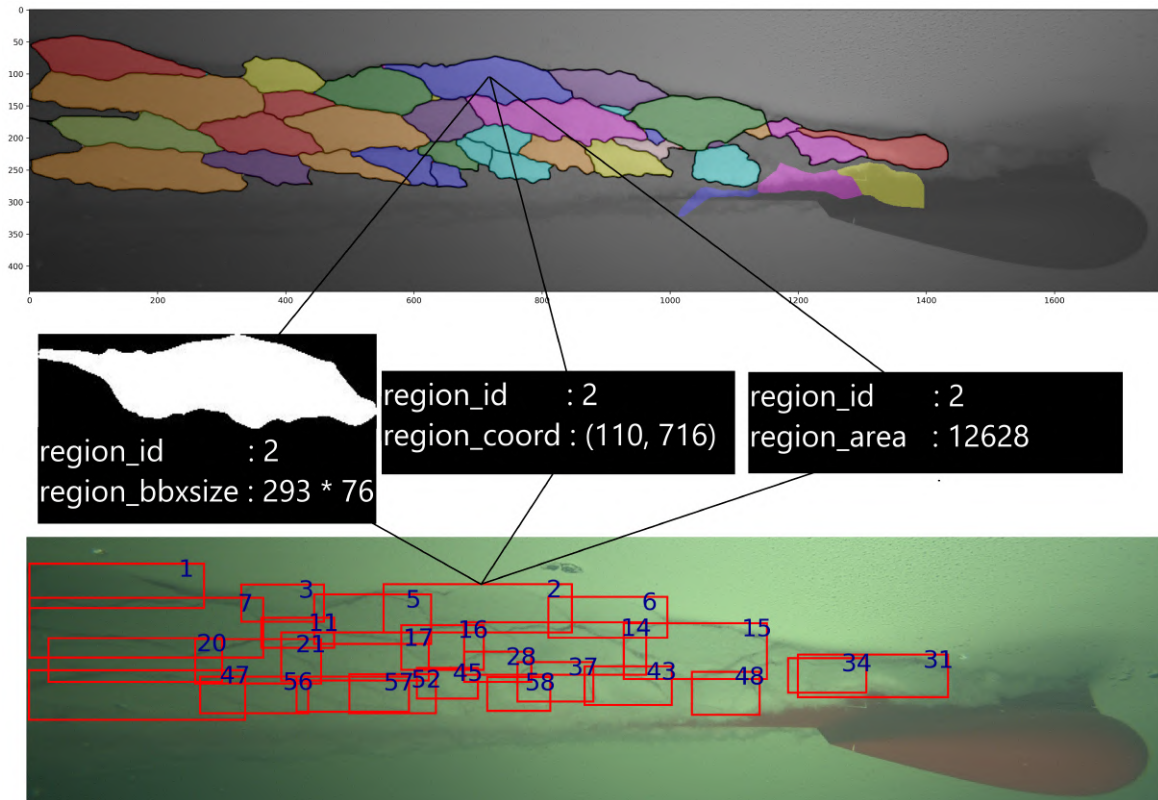


Figure 2.19: Printed information of ice floes for analyzed images

As the image is segmented, each detected region, in other saying each ice floe, is labelled. These labels are then used for identifying ice floes. Although in Figure 2.19 only the ice floe with `region_id : 2` is shown, all the other ice floes are identified in same way. On the left hand side binary image of the ice flow can be seen. This individual images allows the visual inspection on geometry of the broken ice floe. Also they are saved in same size as their bounding boxes. That means axis-aligned aspect ratios of the ice floes can be calculated easily. For instance ice floe with `region_id : 2` has 293×76 pixel size and that means aspect ratio of this particular ice floe is 3.86. In addition to that, this visual information regarding ice floes' geometry allows checking accuracy of the segmentation manually when it is needed.

In middle coordinates of the centroid of the ice floe is given. This coordinate information is given in terms of local coordinate system which takes upper left corner of the image as reference origin. Since every each pixel in this region is already located, this coordinates can also be taken for extreme points of the ice floe.

On the right hand side area information of corresponding ice floe is shown. It is important

to remember at this point that any dimensional information given by the computer will be in terms of pixels. That means this information to be useful, it will be necessary to convert pixel wise data into metric system.

In addition to printed and stored information above, there are bunch of other information for detected ice floes already available. Depending on focus of the research, these properties presented below could be printed in instead of or in addition to the ones presented in this section.

```
1
2
3 def regionprops(label_image, intensity_image=None, cache=True,
4                 coordinates=None):
5 Notes
6         -----
7     The following properties can be accessed as attributes or keys for
8     each of labelled image region:
9
10    **area** : int
11              Number of pixels of the region.
12    **bbox** : tuple
13              Bounding box ``(min_row, min_col, max_row, max_col)``.
14              Pixels belonging to the bounding box are in the half-open
15              interval
16    **bbox_area** : int
17              Number of pixels of bounding box.
18    **centroid** : array
19              Centroid coordinate tuple ``(row, col)``.
20    **convex_area** : int
21              Number of pixels of convex hull image, which is the smallest
22              convex
23              polygon that encloses the region.
24    **convex_image** : (H, J) ndarray
25              Binary convex hull image which has the same size as bounding box
26              .
27    **coords** : (N, 2) ndarray
28              Coordinate list ``(row, col)`` of the region.
```

```

25  **eccentricity** : float
26      Eccentricity of the ellipse that has the same second-moments as
the
27      region.
28  **equivalent_diameter** : float
29      The diameter of a circle with the same area as the region.
30  **euler_number** : int
31      Euler characteristic of region.
32  **extent** : float
33      Ratio of pixels in the region to pixels in the total bounding
box.
34      Computed as ''area / (rows * cols)''
35  **filled_area** : int
36      Number of pixels of the region will all the holes filled in.
Describes
37      the area of the filled_image.
38  **filled_image** : (H, J) ndarray
39      Binary region image with filled holes which has the same size as
40      bounding box.
41  **image** : (H, J) ndarray
42      Sliced binary region image which has the same size as bounding
box.
43  **inertia_tensor** : (2, 2) ndarray
44      Inertia tensor of the region for the rotation around its mass.
45  **inertia_tensor_eigvals** : tuple
46      The two eigen values of the inertia tensor in decreasing order.
47  **intensity_image** : ndarray
48      Image inside region bounding box.
49  **label** : int
50      The label in the labeled input image.
51  **local_centroid** : array
52      Centroid coordinate tuple ''(row, col)'', relative to region
bounding
53      box.
54  **major_axis_length** : float
55      The length of the major axis of the ellipse that has the same
56      normalized second central moments as the region.
57  **max_intensity** : float
58      Value with the greatest intensity in the region.

```

```

59  **mean_intensity** : float
60      Value with the mean intensity in the region.
61  **min_intensity** : float
62      Value with the least intensity in the region.
63  **minor_axis_length** : float
64      The length of the minor axis of the ellipse that has the same
65      normalized second central moments as the region.
66  **moments** : (3, 3) ndarray
67      Spatial moments up to 3rd order
68  **moments_central** : (3, 3) ndarray
69      Central moments (translation invariant) up to 3rd order
70  **moments_hu** : tuple
71      Hu moments (translation, scale and rotation invariant).
72  **moments_normalized** : (3, 3) ndarray
73      Normalized moments (translation and scale invariant) up to 3rd
74      order
75  **orientation** : float
76      In 'rc' coordinates, angle between the 0th axis (rows) and the
77      major
78      axis of the ellipse that has the same second moments as the
79      region,
80      ranging from ' $-\pi/2$ ' to ' $\pi/2$ ' counter-clockwise.
81
82      In 'xy' coordinates, as above but the angle is now measured from
83      the
84      "x" or horizontal axis.
85  **perimeter** : float
86      Perimeter of object which approximates the contour as a line
87      through the centers of border pixels using a 4-connectivity.
88  **slice** : tuple of slices
89      A slice to extract the object from the source image.
90  **solidity** : float
91      Ratio of pixels in the region to pixels of the convex hull image
92      .
93  **weighted_centroid** : array
94      Centroid coordinate tuple ``(row, col)`` weighted with intensity
95      image.
96  **weighted_local_centroid** : array
97      Centroid coordinate tuple ``(row, col)`` , relative to region

```

```

bounding
93     box, weighted with intensity image.
94     **weighted_moments** : (3, 3) ndarray
95         Spatial moments of intensity image up to 3rd order
96     **weighted_moments_central** : (3, 3) ndarray
97         Central moments (translation invariant) of intensity image up to
98         3rd order
99     **weighted_moments_hu** : tuple
100         Hu moments (translation, scale and rotation invariant) of
intensity
101         image.
102     **weighted_moments_normalized** : (3, 3) ndarray
103         Normalized moments (translation and scale invariant) of
intensity
104         image up to 3rd order
105         -----
106         Each region also supports iteration, so that you can do::
107
108     for prop in region:
109         print(prop, region[prop])

```

Listing 2.2: Properties can be achieved for successfully segmented and labelled ice floe regions

2.6 Conversion of the pixel based values into the metric system

Results obtained from image analysis so far are pixel wise information. However it is possible to convert this pixel wise information into metric system using some of geometric features established on the model.

There is a checkered pattern drawn along the bow section of the model. Dimensional information regarding square shapes which form this pattern are known and each of these squares are 100×100 mm. This pattern is shown in Figure 2.20 below.

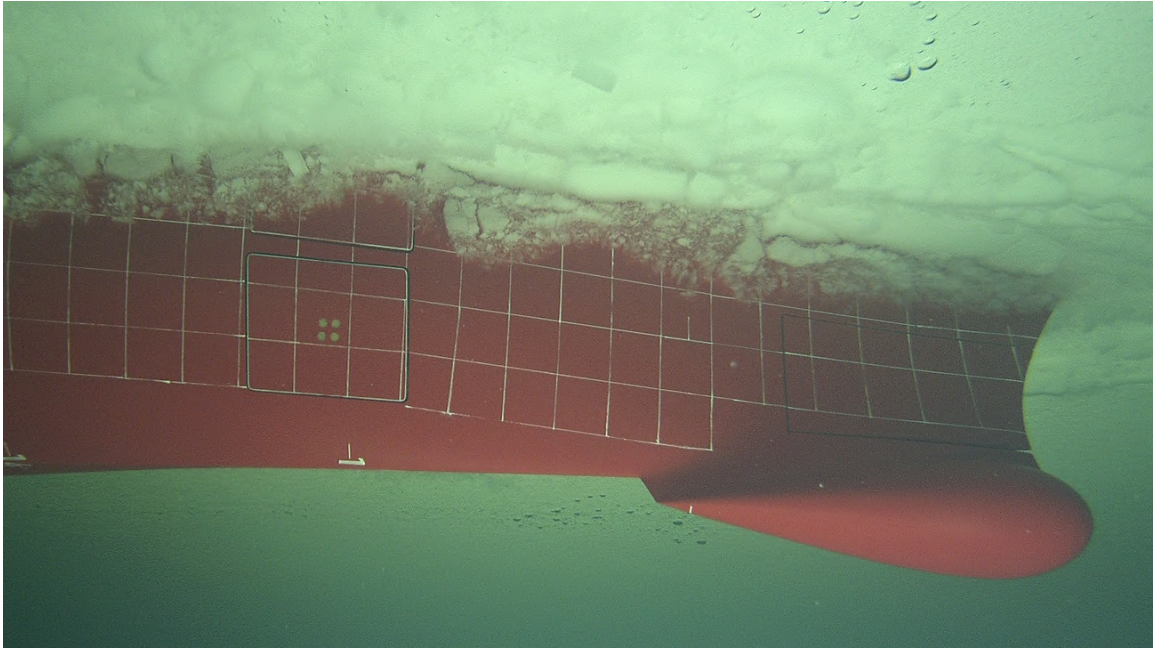


Figure 2.20: Checkered pattern on the model

Another useful information to perform this unit transformation is image properties. Since number of the pixels within any reference length in the image can be known, it is possible to establish how many mm is equivalent of a pixel.

This measurement to make on images can be carried out building up a measurement tool within the algorithm itself. However, Screen Calipers ® tool was used in this study due to its practical usefulness. Underwater recordings were made using wide angle full HD cameras with 1920×1088 resolution. This being the case, conversion between a measured length on the screen and a feature in the image with a known physical dimension becomes an easily applicable approach.

Although the dimensions of the checkered pattern is known, small deviations due to the camera is not placed parallel to these squares may occur. To minimize such deviations same edge was subjected to this measurement for each image and equivalent pixel lengths were calculated for each of them.

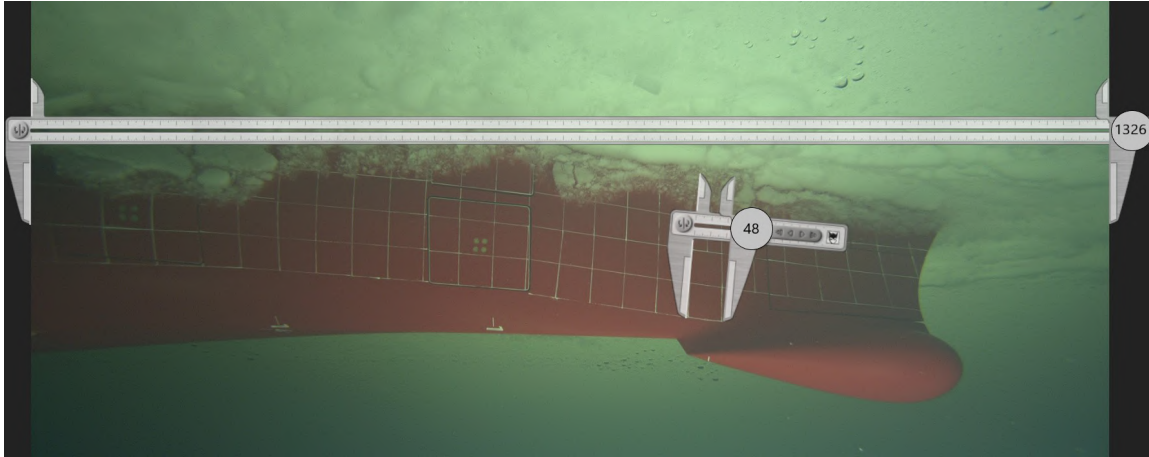


Figure 2.21: Pixel measurement representation

An example screen measurement is shown in Figure 2.21 above. Using this measurement and knowing that pixels in an image are identical with an aspect ratio of 1, area of a pixel can be expressed in metric system. Table 2.6 and 2.7 below shows briefly made conversion for the measurement given.

Number of the pixels measured on screen	Equivalence in metric system
$[-]$	$[mm]$
70	100
1	1.44

Table 2.6: Conversion to real scale, from pixel length to mm

Area of a pixel	Equivalence in metric system
$[pixel^2]$	$[mm^2]$
1	2.07

Table 2.7: Conversion to real scale, from $pixel^2$ to mm^2

2.7 Convergence study regarding number of the images to be evaluated

For the purpose of that understanding necessary amount of images to analyse for each of model speed tested, a convergence study was performed. The purpose of this convergence study is to find a good compromise between the accuracy of the study and the time to be spared to analyze the images.

A randomly selected test run was subjected to this study. It was made by means of analyzing certain amount of images for model speeds 5 and 2 knots and to observing the detected ice floes around bow region. Number and size of the detected ice floes as well as standard deviation were checked in order to see the convergence depending on the number of analyzed images.

Resulting from the convergence study, it was seen that analyzing 4 images from the intervals synchronized with data table for each 5 and 2 knots model speed provides sufficiently good accuracy in results. Convergence behaviour resulted from this study can be seen in Figure 2.22 below.

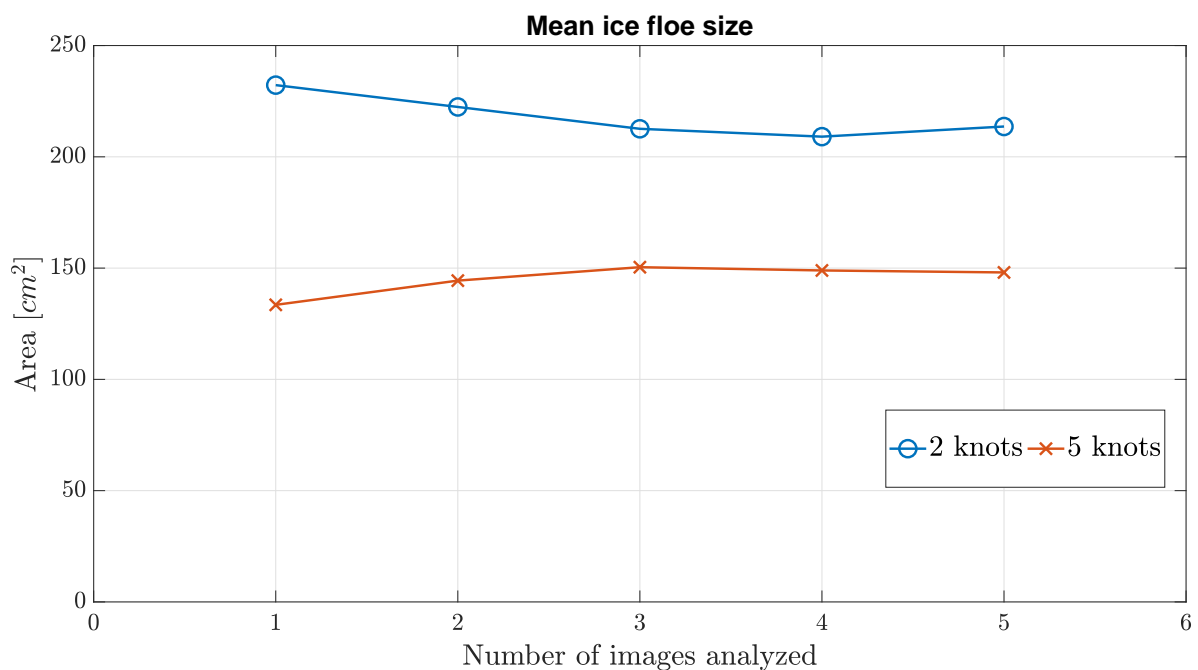


Figure 2.22: Convergence behavior in mean ice floe sizes as number of the images analyzed increases

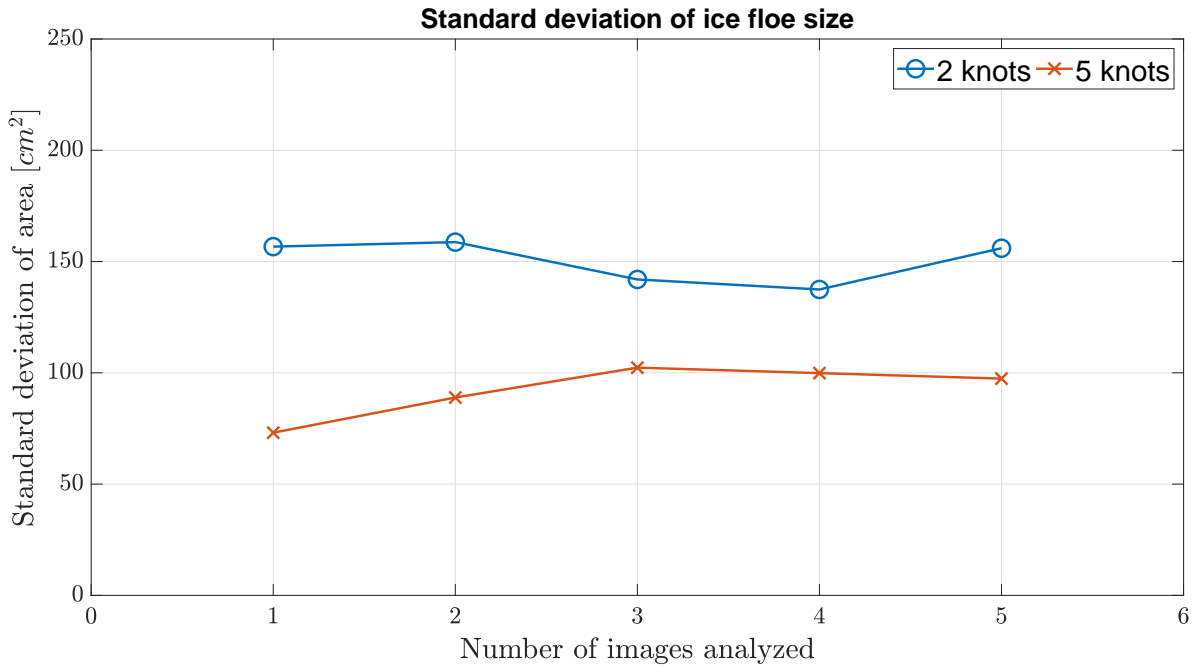


Figure 2.23: Standard deviation in mean ice floe sizes as number of the images analyzed increases

As remaining test runs were analyzed, it was confirmed for them as well that convergence behaviour when 4 images are analyzed is indeed sufficiently accurate.

2.8 Exclusion of incoherent ice floes from the outputs

In order to increase the reliability of the statistics resulting from image analysis, it is important to make sure that outcomes are produced over definitive ice floes within the image. This means that the ice floes with explicitly visible integrity in the region of interest have to be analyzed. Since bow section of the ship model is addressed to be observed, region of interest (ROI) is defined in the way of comprising only bow section. In other saying, ice floes outside of bow section are not desired to incorporate in segmented regions to extract their properties about.

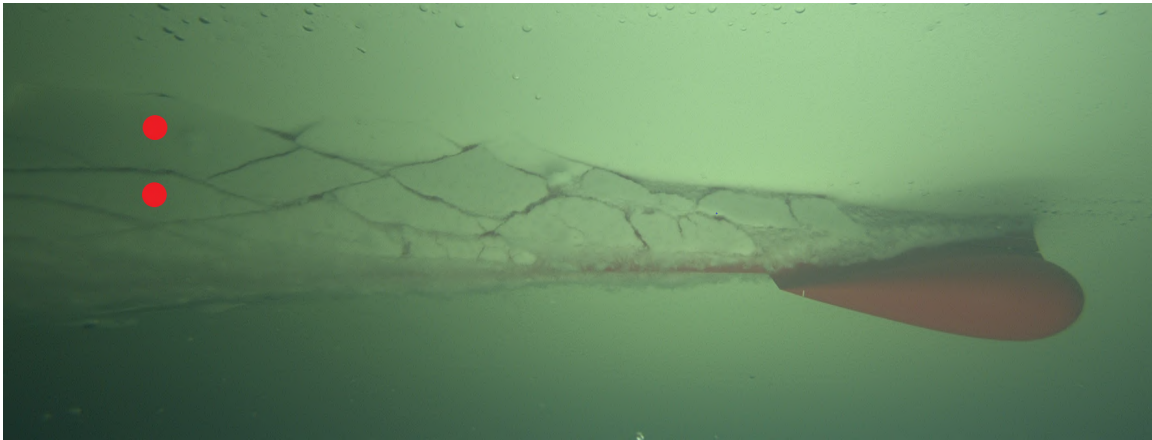
The angle of the second underwater camera that made the recordings used this study was adjusted especially to cover the bow section of the ship model. However, ice breaking process and the motion of the broken ice floes along the model hull are dynamic events.

This being the case, it was observed that some images contain ice floes which are visible within ROI partially or insignificantly due to the limited area that the camera lens can see.

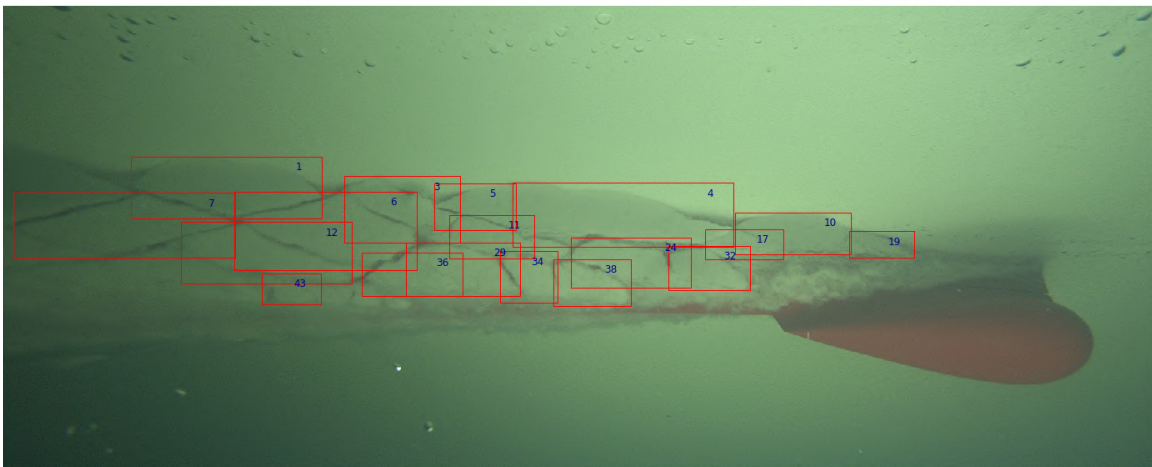
In order to detect such ice floes, previous images to the image to be analyzed have to be checked manually. Thus, one can identify the ice floes which can cause deviations in results. This process is described in Figure 2.24 schematically.



(a) Image to be analyzed



(b) Image before the analyzed one



(c) Analyzed image

Figure 2.24: Checking the ice floes manually around image borderline

Image shown on top (a) is the image to be used as input data in algorithm. Two of the ice floes which are in borderline of the frame are marked with red dot on them for highlighting. At first glance they appear to be within the range of analysis. However, it can be seen checking the previous frame (b) that these ice floes are actually much larger in size than

they appear in the image to analyzed. Given circumstances make it necessary to purge these misleading ice floes from the analysis results.

Finally image (c) on the bottom in Figure 2.24 shows the labelled ice floes in the analyzed image. It can be seen that misleading ice floes marked with red dot are excluded.

When this size difference is insignificantly small, it does not actually cause a sampling error. However, this manual inspection has to be done for each image chosen to analyse in order to decrease the sampling error in results.

2.9 Limitations

This thesis focuses on underwater visual observations of ice floes for a non-typical ice-breaker bow shaped ship model introduced throughout previous chapters. These observations are made for 2 and 5 knots model speeds. In order to have more comprehensive insight, more model speeds can be subjected to image analysis.

Due to the camera positioning and to hull angles, certain amount of keystone effect on the results for especially areas on model with high normal angles are expected. In order to minimize this effect a correction method into the algorithm should be implemented.

During image analyses, it was noted that when the ice floes were found to be very small, the quality of segmentation could decrease. Tiny ice particles covering them, invisibility in their surroundings and limits of the algorithm can lead such consequence for this small pieces in images. This issue can be seen in Figure 2.25 below. In connection with this, ice floes determined to have an area of less than 2000 pixels were excluded from the results.

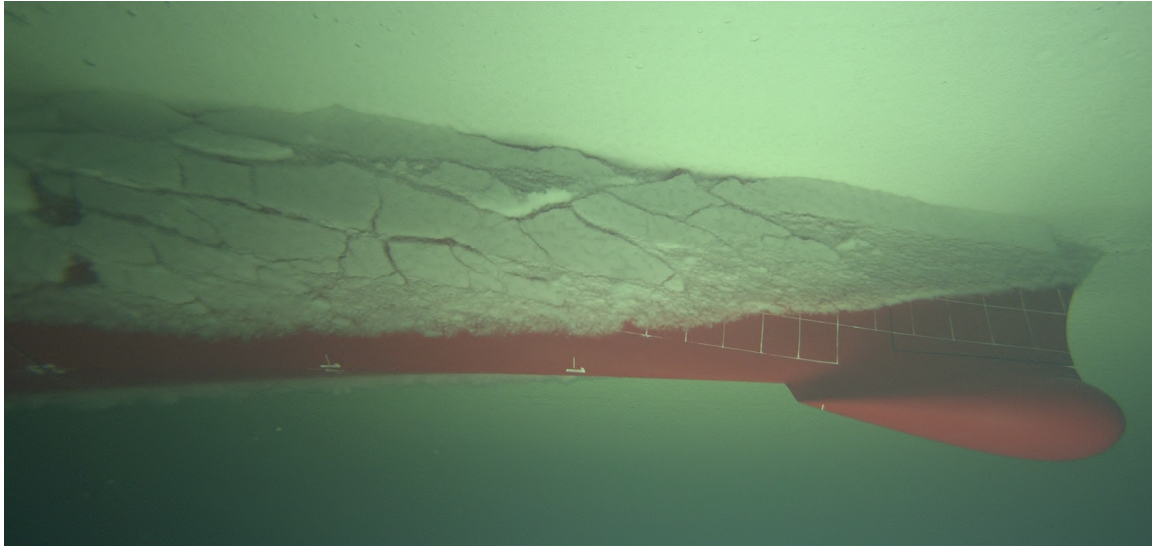


Figure 2.25: Tiny ice particles formed along bow region as model crushes the level ice sheet

Chapter 3

RESULTS

In this section the results of the visual observations done by means of analyzed images for 2 and 5 knots model speed are discussed. These observations coming from underwater recordings mainly include quantitative analyses related to ice floe sizes and numbers. These are to be called ice floe characteristics and change in these characteristics with respect to changes in test parameters are compared. Additionally, these ice characteristics are also compared with the resistance in the bow region which was measured at HSVA in the earlier phases of the research. These comparisons are made to determine the relationships, if any, between this study and those previously performed by the HSVA.

In this chapter, results regarding ice floe characteristics are presented in model scale whereas test parameters are given in full scale.

3.1 Correlation of ice floe characteristics on test variables

Change in ice floe characteristics as test parameters were changed between test runs are analysed in following subsections.

3.1.1 Correlation between ice floe characteristics and model speed

Effect of the change in model speed on floe characteristics are subjected to review looking through ice floe sizes and number of the ice floes formed. This investigation is done for two draught values $T = 5.15 \text{ m}$ and $T = 10.15 \text{ m}$ disjointly. Within each draught value, variation of ice floe characteristics depending on change in speed over ice thickness values tested are presented.

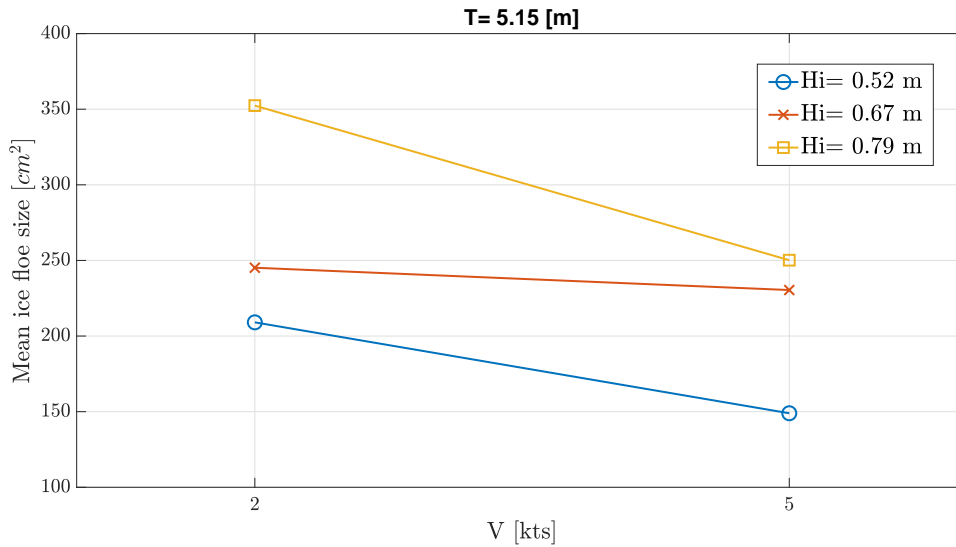
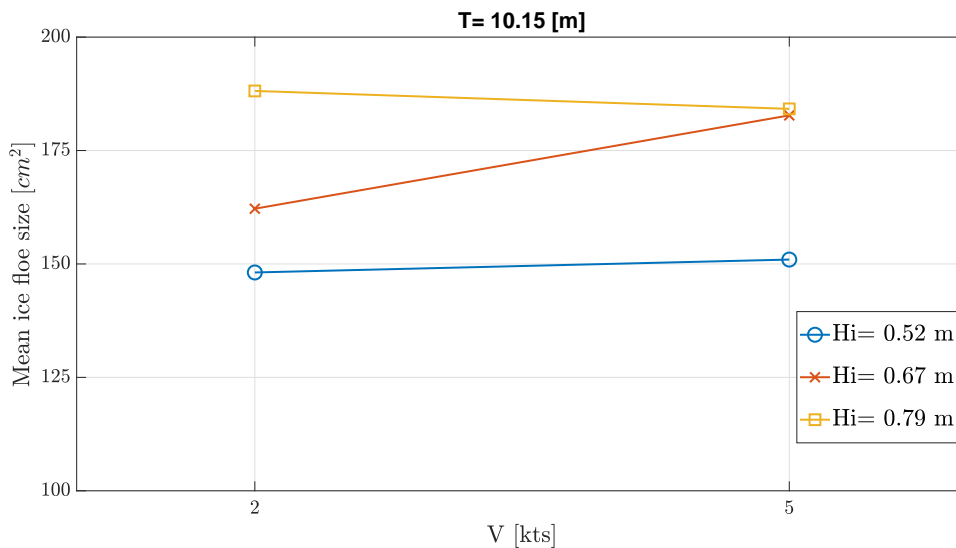
(a) Correlation for $T = 5.15 m$ (b) Correlation for $T = 10.15 m$

Figure 3.1: Correlation between mean ice floe size and model speed

Figure 3.1 above shows mean values of resultant ice floe sizes in which (a) is on the top for $T = 5.15 m$ and (b) is on bottom for $T = 10.15 m$.

Figure 3.1 (a) shows that as model speed increases from $V = 2 kts$ to $V = 5 kts$, mean ice floe sizes tend to decrease for each ice thickness values tested. In other saying as model speed increases smaller ice floes form during ice breaking process. It is observed for this particular ship model that the median ice thickness seemed less reactive to the change in speed than the thick and thin ones tested. Percentage change in floe sizes between model speeds 2 and 5 kts is measured as 6% for median thickness whereas is as 29% for other two.

Regardless of model speed values presented, ice floes tend to be greater as ice thickness increases. This observation resulting from image analysis is in parallel with the formulation given regarding the cusp length, Lindqvist 1989.

$$l_c = \left(E \times H_{ice}^3 / (12 \times (1 - v^2) \times \rho_w \times g) \right)^{0.25} \quad (3.1)$$

Where E is Youngs modulus, v is the poisson coefficient, ρ_w is the density of water and g is the gravitational constant. Based on the formulation, the length of the cusps increases in direct proportion to $H^{3/4}$. This also means ice floe size dependency on ice thickness and thus the larger the ice thickness, the larger the expected mean floe size.

Figure 3.1 (b) shows that ice floes tend to be greater as ice thickness increases for each of model speeds as it is the case with $T = 5.15 \text{ m}$. However it is not confirmed for this given draught $T = 10.15 \text{ m}$ that change in model speed leads a significant rate of changes in floe sizes, unlike $T = 5.15 \text{ m}$. Although level ice thickness $Hi = 0.67 \text{ m}$ differs from other two, this alteration may occur due to random errors in experiment and not enough to draw a global behaviour.

It is observed in between draught values $T = 5.15 \text{ m}$ and $T = 10.15 \text{ m}$ that largest average floe size differs drastically when model speed is 2 kts . Such significant difference in largest average floe size in between $T = 5.15 \text{ m}$ and $T = 10.15 \text{ m}$ is not observed when model speed is 5 kts .

This may be resulting from that the slower the model speed, the higher the noticeability of the effect of hull angles. Although stem angle is high, normal angles of the model decreases after bow entrance region. Since this increases bending effect, greater ice floes may be formed when model speed is smaller and crushing at bow is minimized.

Figure 3.2 below shows mean values of ice floe numbers observed in which (a) is on the top for $T = 5.15 \text{ m}$ and (b) is on bottom for $T = 10.15 \text{ m}$.

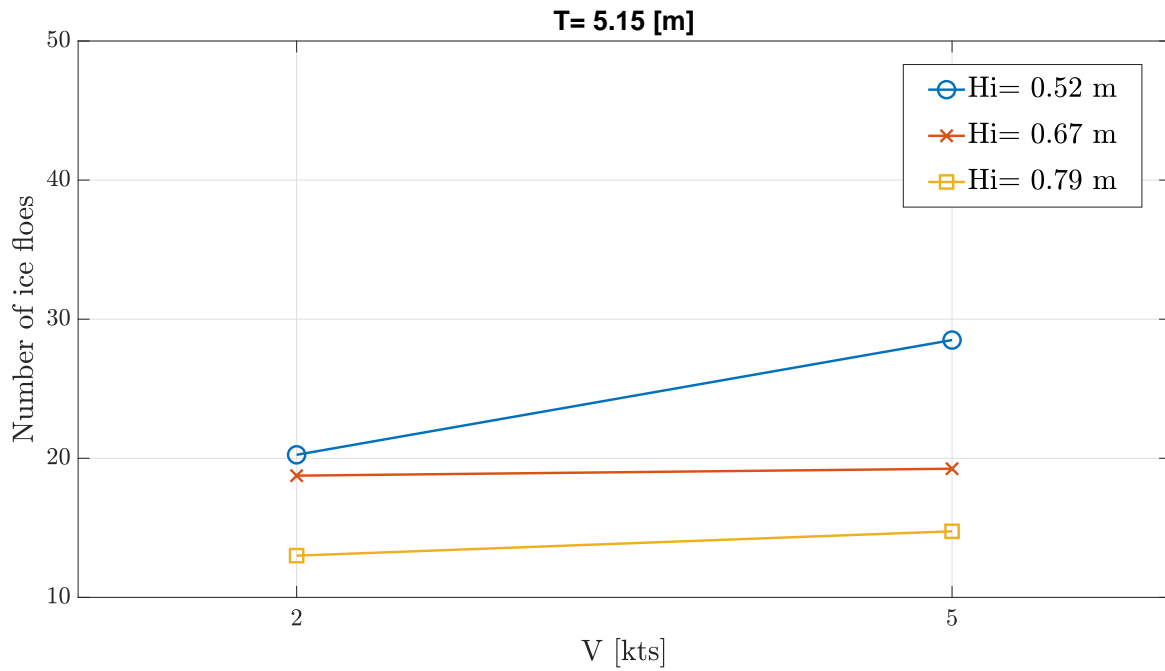
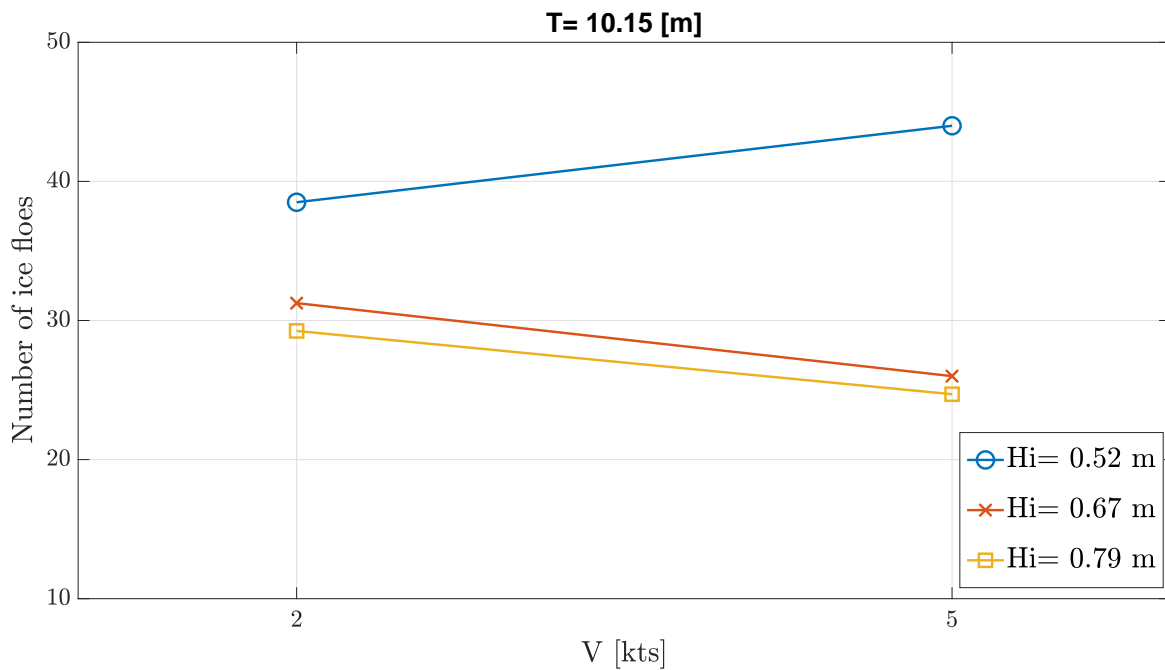
(a) Correlation for $T = 5.15 m$ (b) Correlation for $T = 10.15 m$

Figure 3.2: Correlation between ice floe number and model speed

Figure 3.2 (a) shows that increase in model speed resulted in more ice floes for each thickness value under the condition that $T = 5.15 m$. However these rates of increase are not significant other than for $H_i = 0.52 m$.

It is seen in Figure 3.2 (b) that number of ice floes for $T = 10.15 m$ increased only

for $H_i = 0.52 \text{ m}$ as model speed increases whereas they decrease for $H_i = 0.67$ and $H_i = 0.79 \text{ m}$. Thus a generalisation for ice floe formation can not be made based on the data shown for $T = 10.15 \text{ m}$.

For both draught values $T = 5.15 \text{ m}$ and $T = 10.15 \text{ m}$, model behaves similarly when model speed changes for thickness value $H_i = 0.52 \text{ m}$ unlike when it is $H_i = 0.67$ and $H_i = 0.79 \text{ m}$. This singular behaviour may be related to the level ice properties for this particular level ice thickness. However, more model speed data is required in order to better understand the model speed dependent behavior of ice floe numbers.

3.1.2 Correlation between ice floe characteristics and level ice thickness

Effect of the change in level ice thickness on floe characteristics are subjected to examination looking through ice floe sizes and number of the ice floes observed per 100 cm^2 of ice covered area. It was thought that the ice floe coverage related information may give more insight than investigating only the ice floe numbers due to the sliding component is affected by ice coverage directly.

Within each draught value, variation of ice floe characteristics depending on level ice thickness over model speed values tested are presented. Linear regression for each data set is then performed in order to see the trends.

Figure 3.3 below shows relation between mean ice floe sizes and level ice thickness values tested in which (a) is on the top for $T = 5.15 \text{ m}$ and (b) is on bottom for $T = 10.15 \text{ m}$.

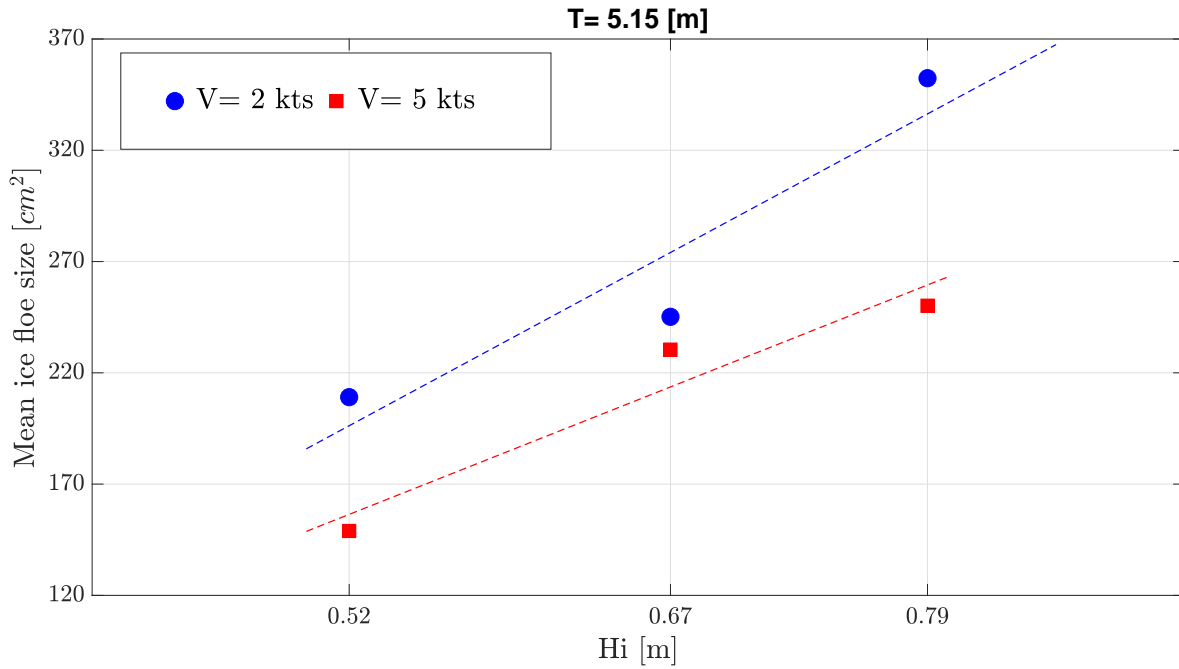
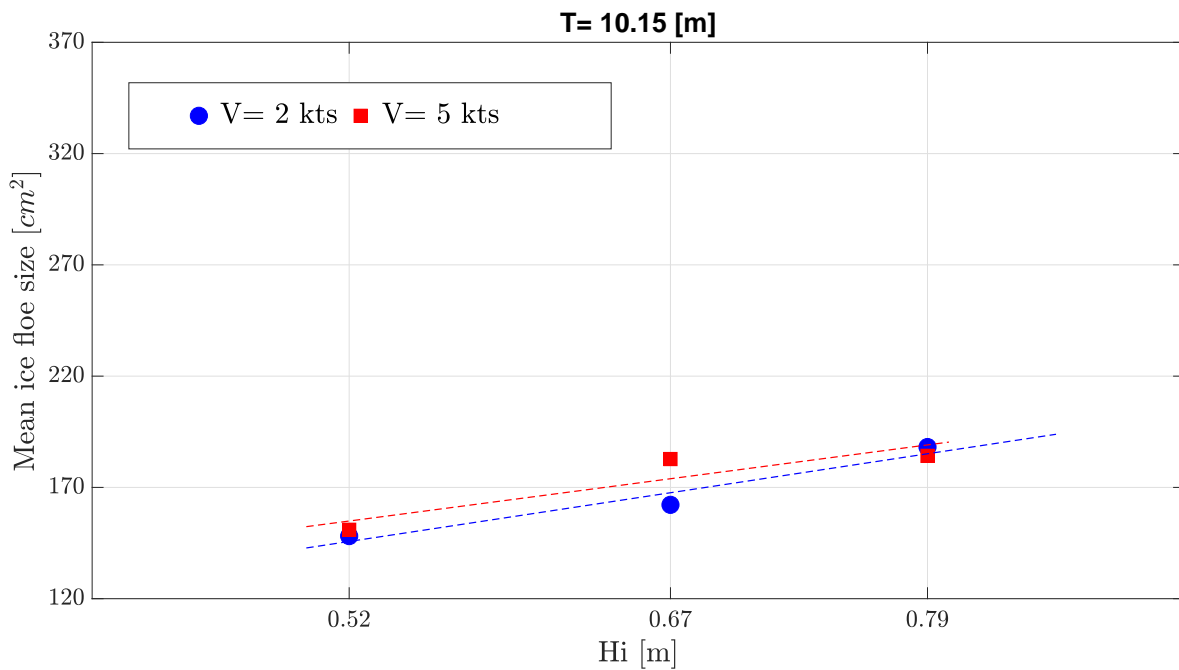
(a) Correlation for $T = 5.15 m$ (b) Correlation for $T = 10.15 m$

Figure 3.3: Correlation between mean ice floe size and level ice thickness

It is observed for both draught conditions that the model tends to form bigger ice floes as level ice thickness increases. This increasing trend is observed for both model speeds 2 and 5 *kts* analyzed.

Figure 3.3 (b) shows that increasing trends and mean ice floe sizes are fairly similar for 2

and 5 *kts* indiscriminatingly. It is also seen that the scatter and the slope of the trends are quite similar. However this similarity in increasing trend seems less alike in Figure 3.3 (a) between them for 2 and 5 *kts*. It is explicitly seen for $T = 5.15\text{ m}$ that ice breaking process at 2 *kts* results in larger ice floes than at 5 *kts*. Additionally, rate of increase and mean ice floe sizes are much higher for $T = 5.15$ than for $T = 10.15\text{ m}$.

These differences in results for different test parameters tested are possibly lead by different ice breaking mechanisms take place based upon hull angles and by different beams at waterlines. Normal angles of the hull for $T = 5.15\text{ m}$ at stem region is higher than is for $T = 10.15\text{ m}$. However later in outside of the stem area, this superiority changes in favor of $T = 10.15\text{ m}$. These more favorable normal angles in lower draught can explain the difference seen between $T = 5.15$ and $T = 10.15\text{ m}$, as they increase the share of bending failure in ice breaking process.

In following Figure 3.4 ice coverage per 100 cm^2 is presented.

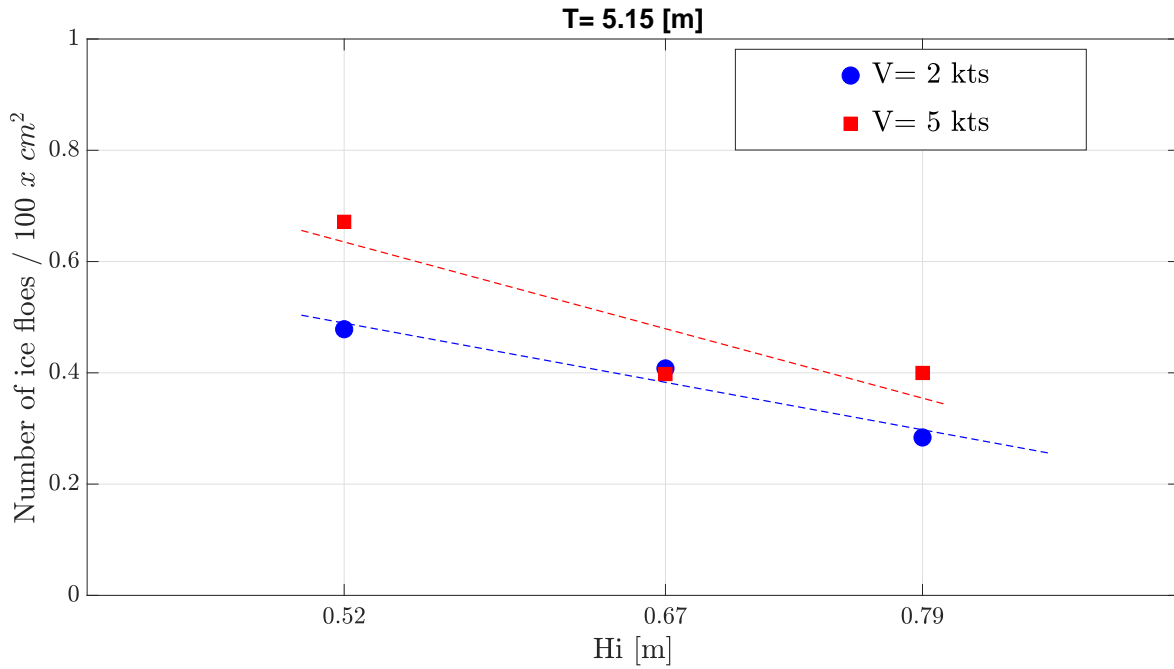
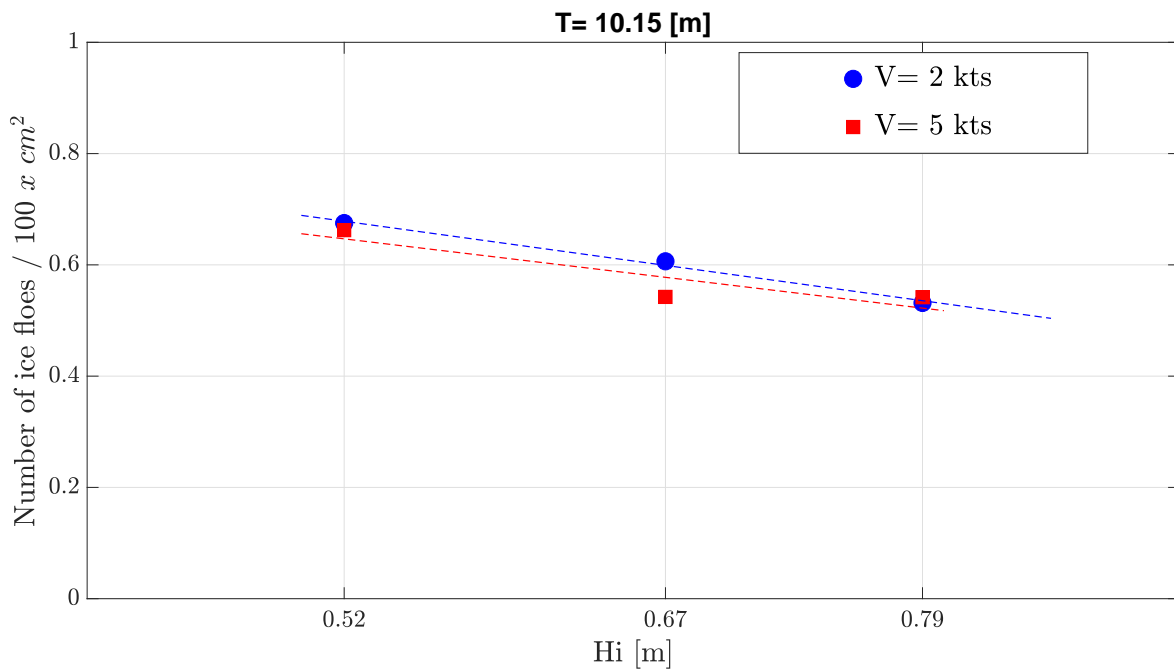
(a) Correlation for $T = 5.15 m$ (b) Correlation for $T = 10.15 m$

Figure 3.4: Correlation between ice floe density and level ice thickness

Quantities of the ice floes per 100 cm^2 for both draught scenarios are observed to be decreased as level thickness values are increased. This decreasing trends are seen for each model speed.

The similarity presented between floe size trends for $T = 10.15 m$ is obtained for floe

density as well. Density of the floes as well as slopes of the trend lines are fairly close to each other for given model speeds.

Although such goodness of fit between model speeds is not obtained for $T = 5.15 m$, slope of the trend lines exhibit impressively same characters when they are compared with their correspondences in Figure 3.3 (a). This consistency in slope of the trend lines between floe densities and floe sizes is achieved for $T = 10.15 m$ as well.

3.1.3 Correlation between ice floe characteristics and hull angle

The dependence of ice floe characteristics on hull normal angles will be discussed in this section. To do this, test parameters are compared disjointly over model speeds. Hull normal angle ψ is calculated based on the Equation 3.2 given below where ψ is normal angle, α is waterline angle and ϕ is buttock angle.

$$\psi = \arctan \left(\frac{\tan \Phi}{\sin \alpha} \right) \quad (3.2)$$

Two limiting lines are drawn in Figure 3.5, in order to show the normal angles for bow section and for imaginary subregion within this. These regions are visualized with a vertical black lines presented. The subregion here is drawn to show and to provide insight where the superiority of normal trunk angles changes between draft scenarios. Right hand side of the first black line is where normal angles for $T = 5.15 m$ are higher while left hand side is where normal angles for $T = 5.15 m$ are smaller.

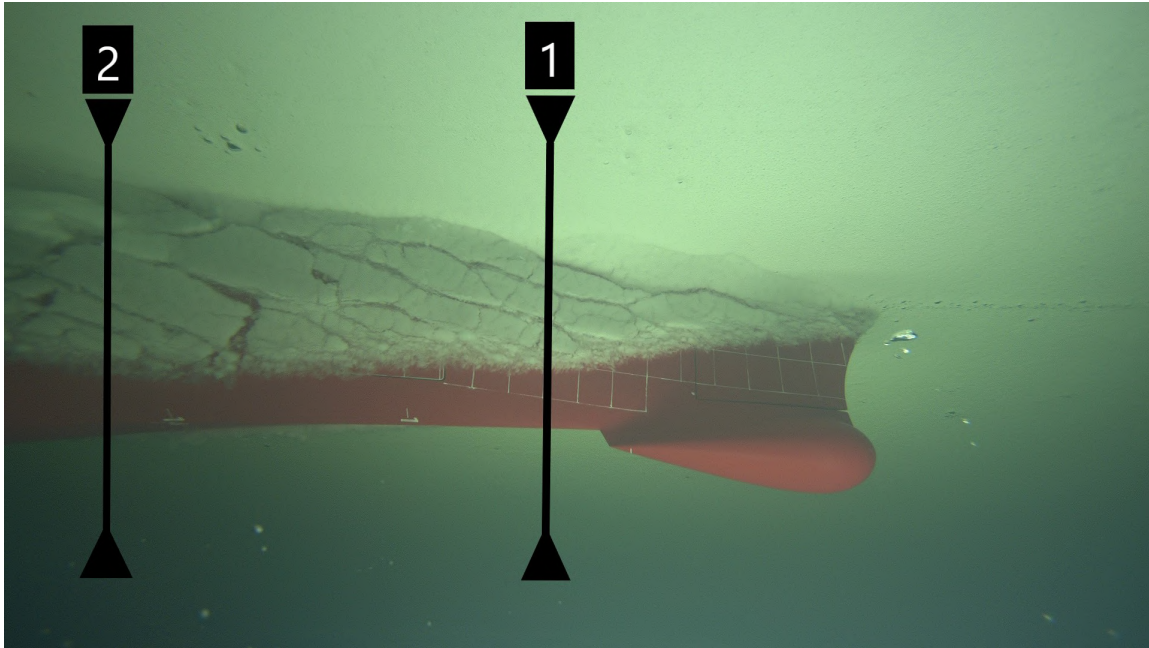


Figure 3.5: Limiting lines for hull angles to be shown

Recalling 2.2, this subregion can be seen including the sections marked B , C , D and E . Thus the average values of hull normal angles ψ for this subregion and for bow section are calculated for $T = 5.15$ and for $T = 10.15$ m.

Draught	Value [m]	Mean normal angle [ψ]	
		from stem to delimiter 1	from stem to delimiter 2
Ballast	5.15	76.07	68.93
Loaded	10.15	64.4	73.24

Table 3.1: Mean normal angles corresponding to the delimiter 1 and 2

Figure 3.6 below shows relation between mean ice floe sizes and hull normal angles ψ corresponding to the bow section for ice thickness values tested.

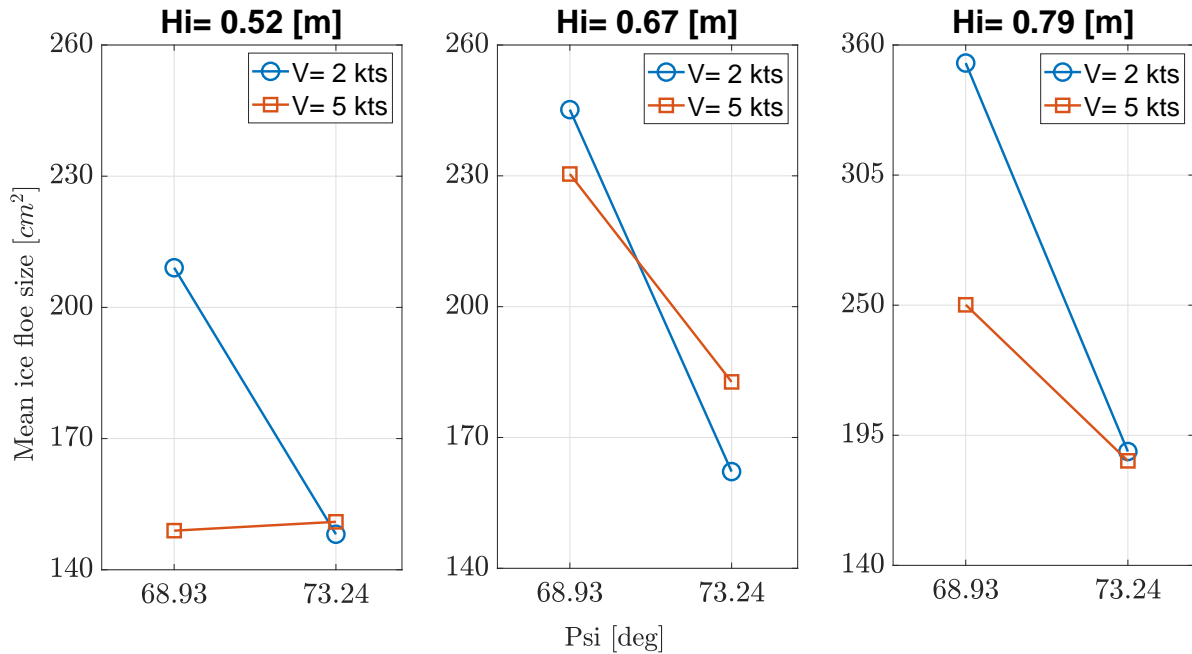


Figure 3.6: Correlation between mean ice floe size and normal angles

It is observed for level ice thickness values tested that smaller ice floes are formed as draught increases from $T = 5.15$ to $T = 10.15$ m. Only exception seem to be for this is $Hi = 0.52$ m - $V = 5$ kts condition. However singularity in this behavior can be resulting from random errors. Greatest drop in ice floe sizes for each test run is observed when model speed is $V = 2$ kts. This observation also confirms the observation made earlier in Section 3.1.1 which is that hull angle effect seems more dominant for model speed $V = 2$ kts than for $V = 5$ kts. It is seen in Figure 3.6 that average normal angles increase from $T = 5.15$ to $T = 10.15$ m. along the bow section. This may have reduced the bending portion in the ice breaking process, resulting in smaller ice floes.

Figure 3.7 is presented in order to visualize the hull normal angle ψ and ice floe size relation mentioned above. Image (a) on top corresponds to $T = 5.15$ m - $V = 2$ kts - $Hi = 0.69$ m whereas , image (b) below corresponds to $T = 10.15$ m - $V = 2$ kts - $Hi = 0.69$ m. Thus it is possible to compare the hull angle effect since the only parameter differs is draught values.

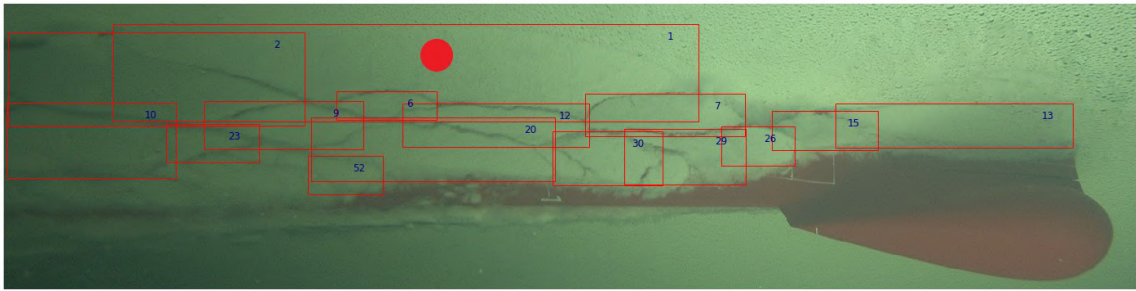
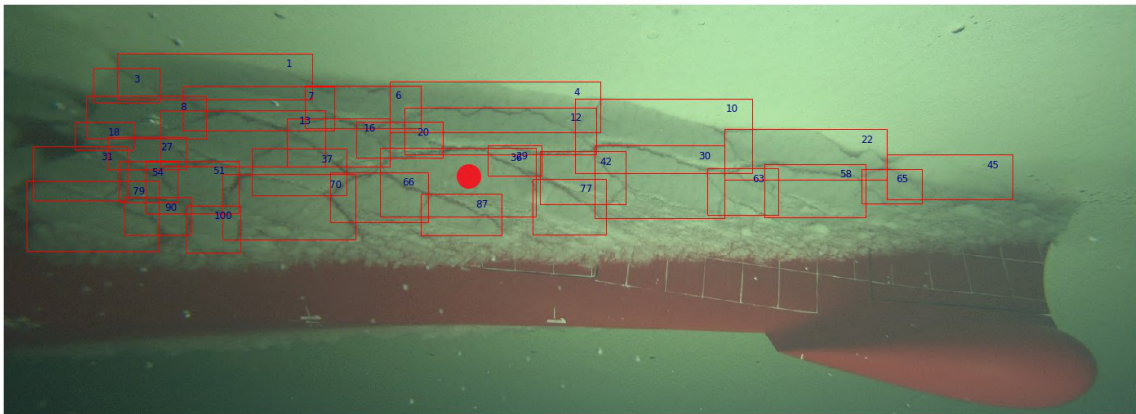
(a) $T = 5.15 \text{ m} - V = 2 \text{ kts} - Hi = 0.69$ (b) $T = 10.15 \text{ m} - V = 2 \text{ kts} - Hi = 0.69 \text{ m}$

Figure 3.7: Sample comparison of the greatest ice floes formed between lower and higher draughts

Red dots in each image shows the greatest ice floes detected. The size of the greatest ice floe in Figure 3.7 (a) is estimated about 1580 cm^2 . It can be seen that this floe was formed at waterline level and has high axis aspect ratio. This is a good example of bending induced ice failure. As for in Figure 3.7 (b), the greatest ice floe is estimated about 355 cm^2 which is much smaller than the one in (a).

More interestingly, both of the ice floes shown are about at the same longitudinal position along bow section which corresponds to the sections $H-G$ presented in Figure 2.2. Normal angle is calculated in this section as $\psi = 54.87^\circ$ for lower draught while is $\psi = 74.96^\circ$ for higher draught. This observations seems to be supporting the mechanism mentioned regarding increased bending portion.

Figure 3.8 below shows relation between floe densities for given unit area and hull normal angles ψ corresponding to the bow section for ice thickness values tested.

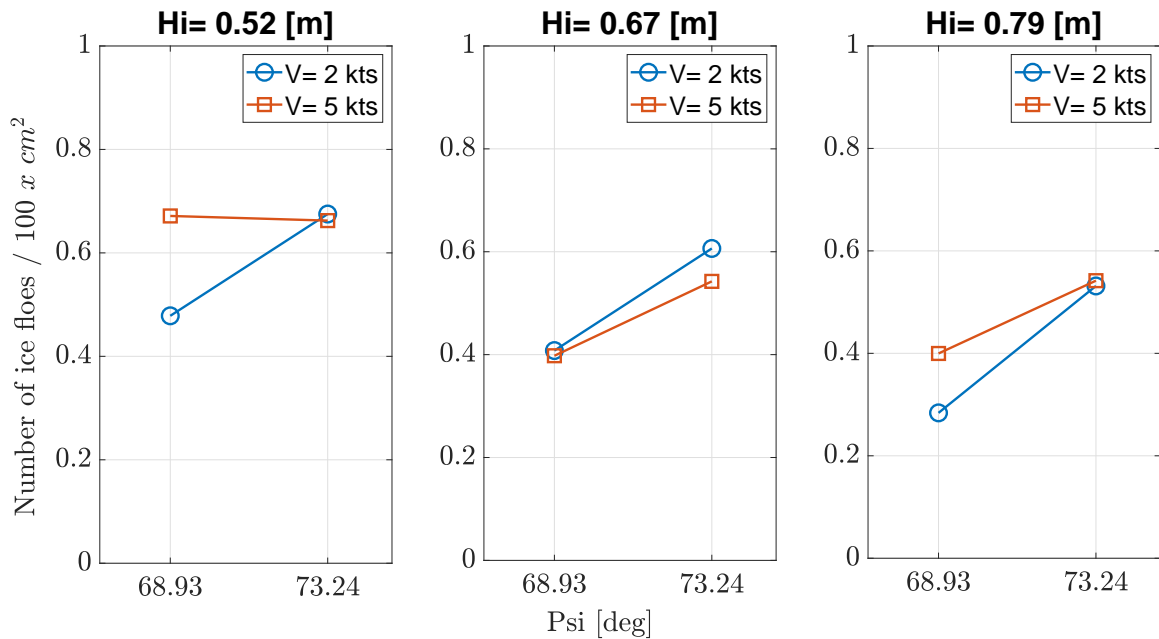


Figure 3.8: Correlation between ice floe densities and normal angles

Figure 3.7 can also be referred for representing the ice floe densities with respect to normal angles. It is observed that number of the ice floes per square centimeter of ice covered areas increase in parallel to the increase in normal angle of the hull. Although ice coverage values for both images (a) and (b) are not significantly differing from each other, number of the floes observed for higher draught is considerably higher than is for lower draught. This results in greater ice floe densities for higher draught scenarios tested, with the exception of $H_i = 0.52 \text{ m} - V = 5 \text{ kts}$ condition once again.

3.1.4 Ice coverage around bow section

Due to the fact that ice covered areas induce sliding resistance, total ice coverage values in bow section based on ice floes detected are calculated. This investigation is done for both of draught values $T = 5.15 \text{ m}$ and $T = 10.15 \text{ m}$ disjointly and presented in Figure 3.9.

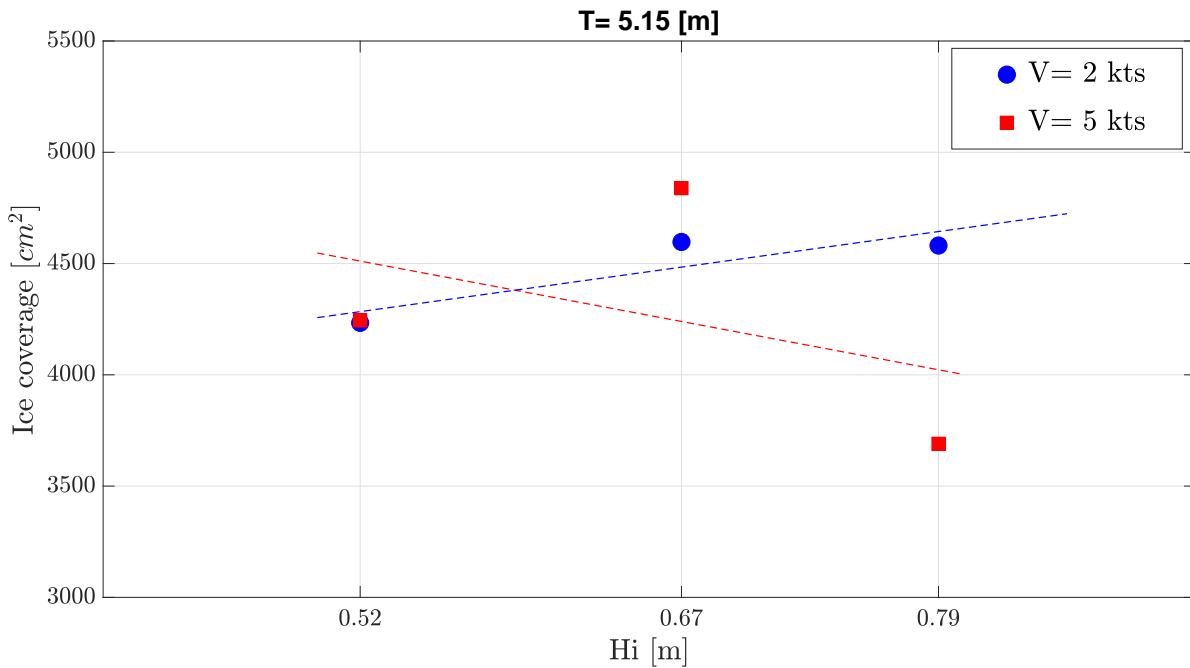
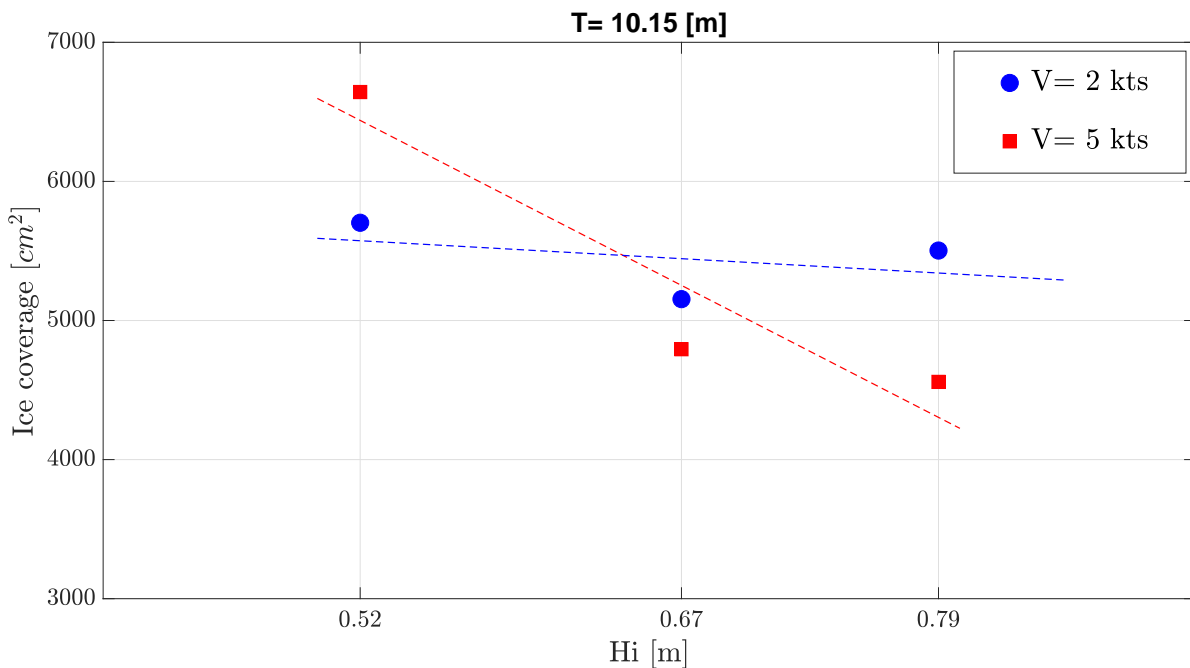
(a) Ice coverage values for $T = 5.15\text{ m}$ (b) Ice coverage values for $T = 10.15\text{ m}$

Figure 3.9: Ice coverage dependency over level ice thickness values tested

It is observed for model speed $V = 5\text{ kts}$ that ice coverage trends for both draught values look similar. However, a general behavior regarding ice coverage in bow section can not be drawn with the data available. Also real ice coverage values for each case is expected to be slightly higher than the calculated values knowing that correction over floe sizes due to

3D effect is not performed in this study and to exclusion of tiny ice floes/particles during image analysis.

On the other hand, wetted surface area is visibly higher for $T = 10.15\ m$ than for it is for $T = 5.15\ m$. Although this being the case, ice coverage between both draughts are not significantly different between each other except when model is in $Hi = 0.52\ m$.

3.2 Associating the ice floe characteristics with the bow resistance measured on the model

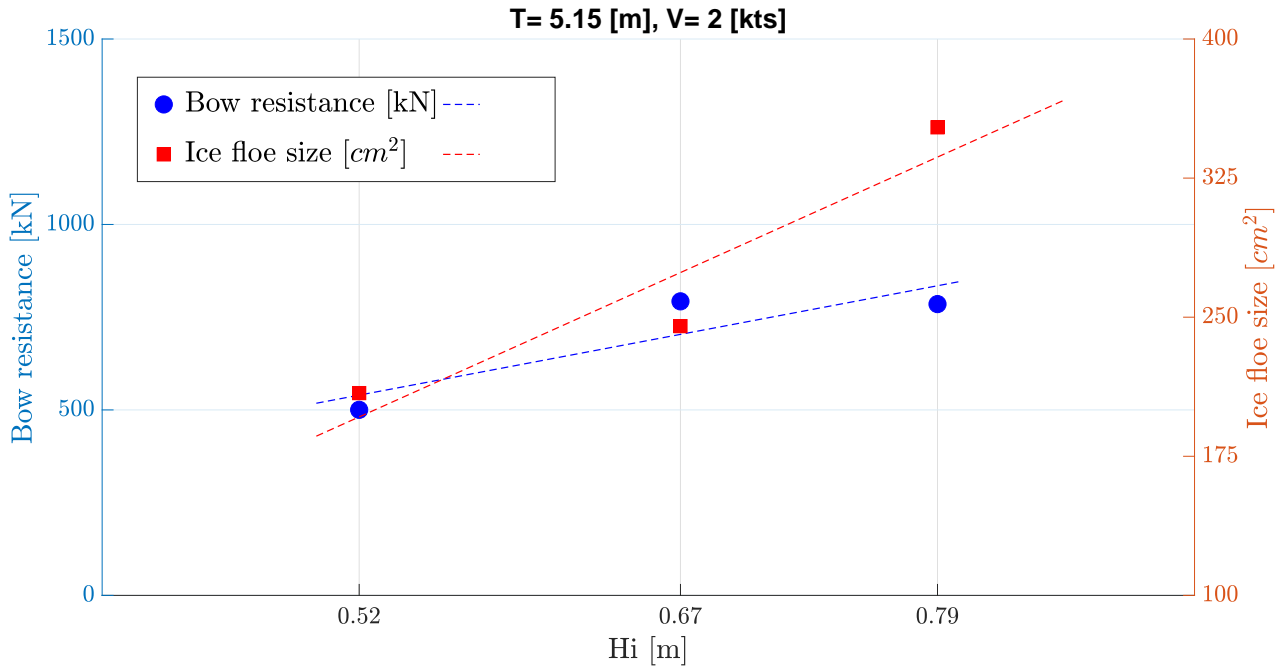
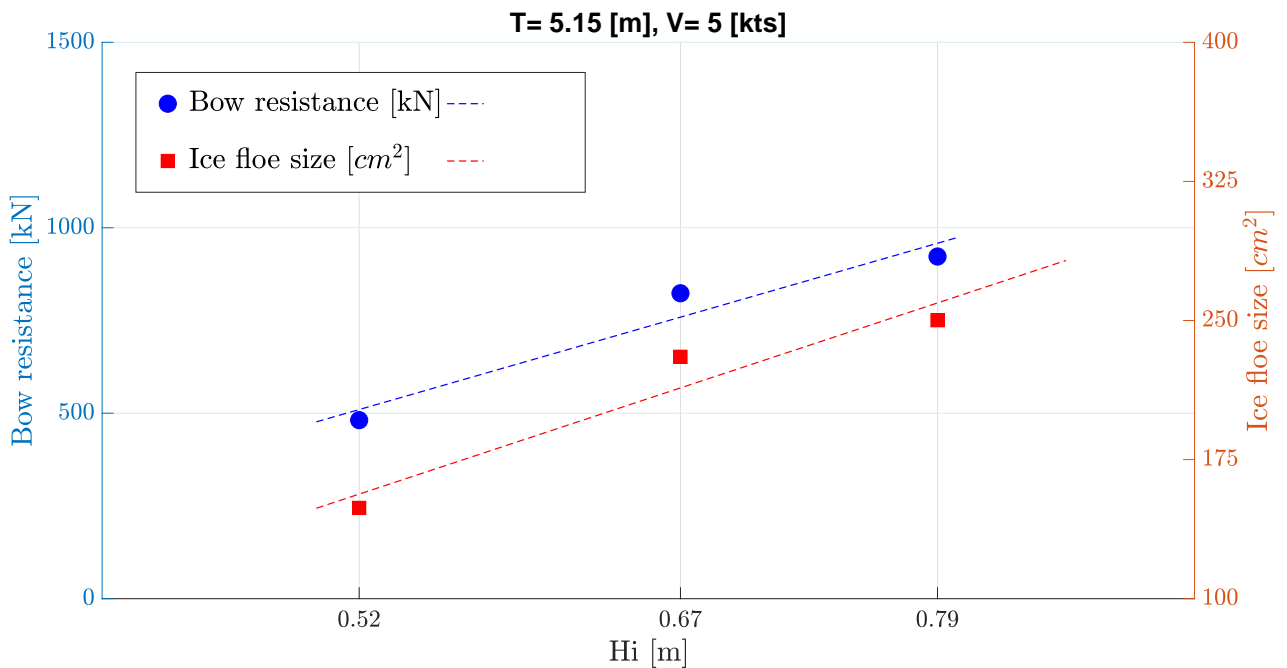
In this chapter, it is aimed to compare the ice floe properties obtained as a result of the image analysis performed with the experimental results of the resistance study of the model carried out by HSVA. To what extend they can be relatable between each other will be discussed in following sections.

Since image analyses done in this study covers only the bow section of the model, comparisons are made with only bow resistance values.

3.2.1 Relation between ice floe characteristics, bow resistance and level ice thickness

Bow resistance values and mean ice floe sizes depending on level ice thickness values tested are presented. Each speed and draught scenarios are investigated individually.

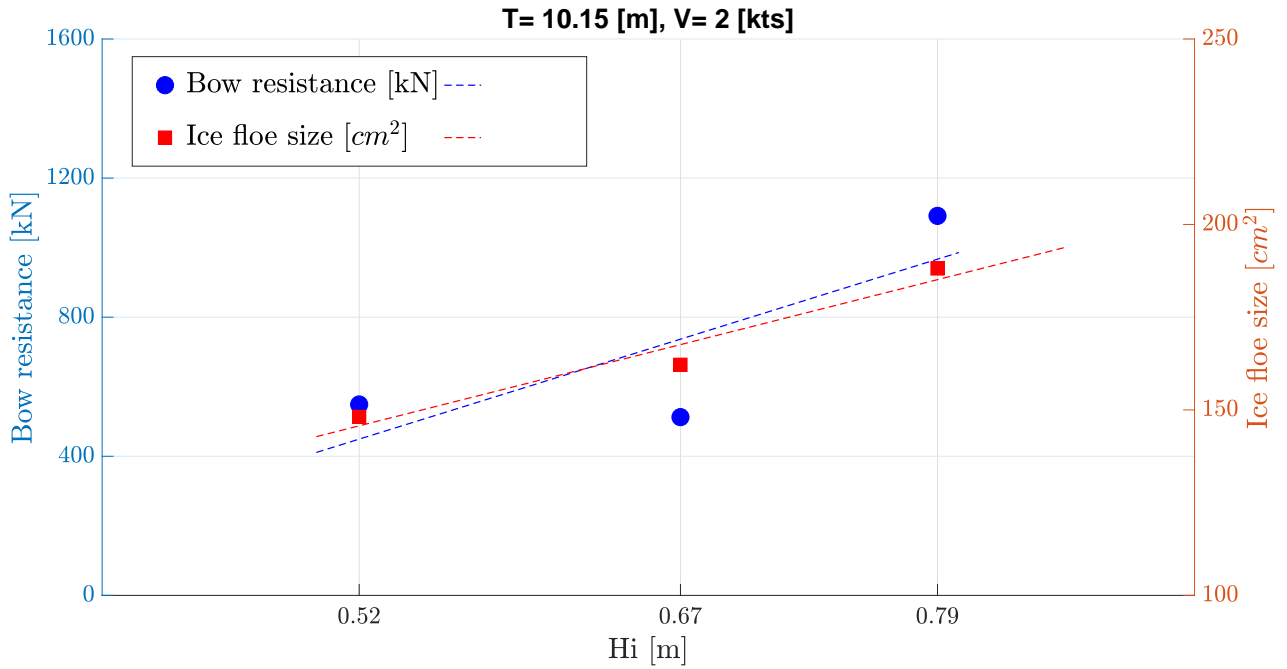
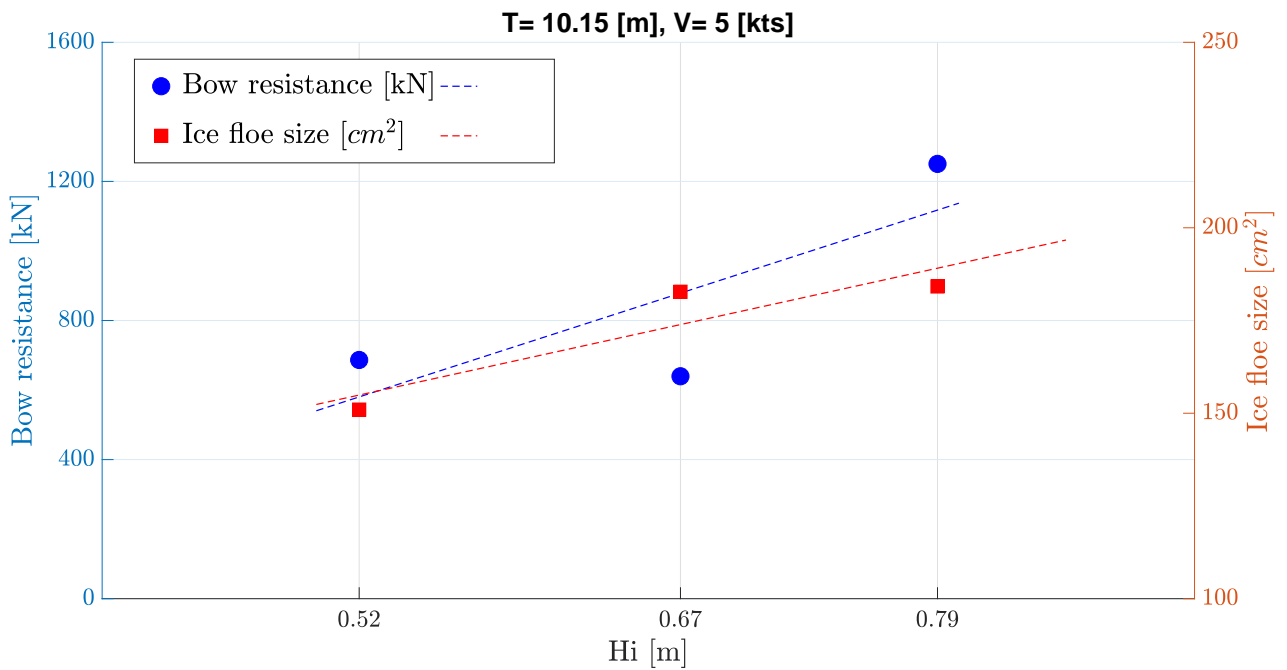
Figure 3.10 shows mean ice floe size - bow resistance comparison for lower draught scenario.

(a) Bow resistance - mean ice floe size relation for $V = 2 \text{ kts}$ (b) Bow resistance - mean ice floe size relation for $V = 5 \text{ kts}$ Figure 3.10: Bow resistance - mean ice floe size relation depending on level ice thickness, $T = 5.15 \text{ m}$

It is observed that both bow resistance values and mean ice floe sizes have increasing trends as level ice thickness increases. Slope of these trends for model speed $V = 2 \text{ kts}$, Figure 3.10 (a), seems tending to be higher in compare with the resistance trend.

Regarding the case with model speed $V = 5 \text{ kts}$, Figure 3.10 (b), it is seen that trends obtained from bow resistance values and ice floe sizes look nearly same. Following these similarity obtained, an inference can be drawn that the bow resistance can be related to ice floes' size for model draught $T = 5.15 \text{ m}$.

Higher draught case is shown in Figure 3.11 below.

(a) Bow resistance - mean ice floe size relation for $V = 2 \text{ kts}$ (b) Bow resistance - mean ice floe size relation for $V = 5 \text{ kts}$ Figure 3.11: Bow resistance - mean ice floe size relation depending on level ice thickness, $T = 10.15 \text{ m}$

As it is the case for lower draught, increasing trends in bow resistance and mean ice floe sizes are observed for higher draught as well. This observation is valid also for both model speeds $V = 2$ and $V = 5 \text{ kts}$.

When we examine the graphs one by one, it is seen that the slopes of the trends are fairly close between each other, so much that almost identical for $V = 2 \text{ kts}$.

In order to see the goodness of the fit for mean ice floe data within bow resistance comparison, coefficients of determination are also checked.

	Draught	Speed	
	$[m]$	2 knots	5 knots
Ballast	5.15	0.93	0.89
Loaded	10.15	0.97	0.78

Table 3.2: $R - squared$ values for the linear regression performed

This intercompatibility obtained between the image analysis performed in this study and resistance study done by HSVA seems confirming the ice floe size and resistance in the bow section of the model tested.

3.2.2 Relation between ice floe characteristics, bow resistance and speed

Bow resistance and ice coverage values depending on model speeds tested are presented. Each level ice thickness and draught scenarios are investigated individually.

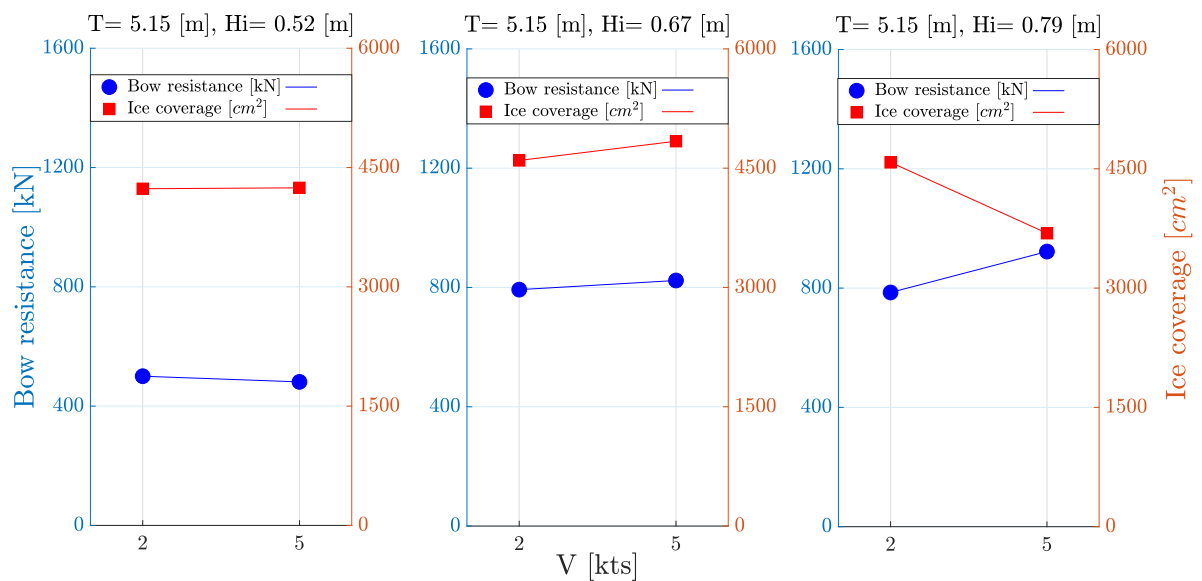


Figure 3.12: Bow resistance - ice coverage depending on model speed, $T = 5.15 \text{ m}$

As the model speed increases from $V = 2$ to $V = 5$ *kts* bow resistance and ice coverage values seem to not changing considerably for level ice thickness $Hi = 0.52$ and $Hi = 0.67$ *m*. However, this changes for $Hi = 0.79$ *m* in the way that bow resistance increases noticeably whereas ice coverage decreases.

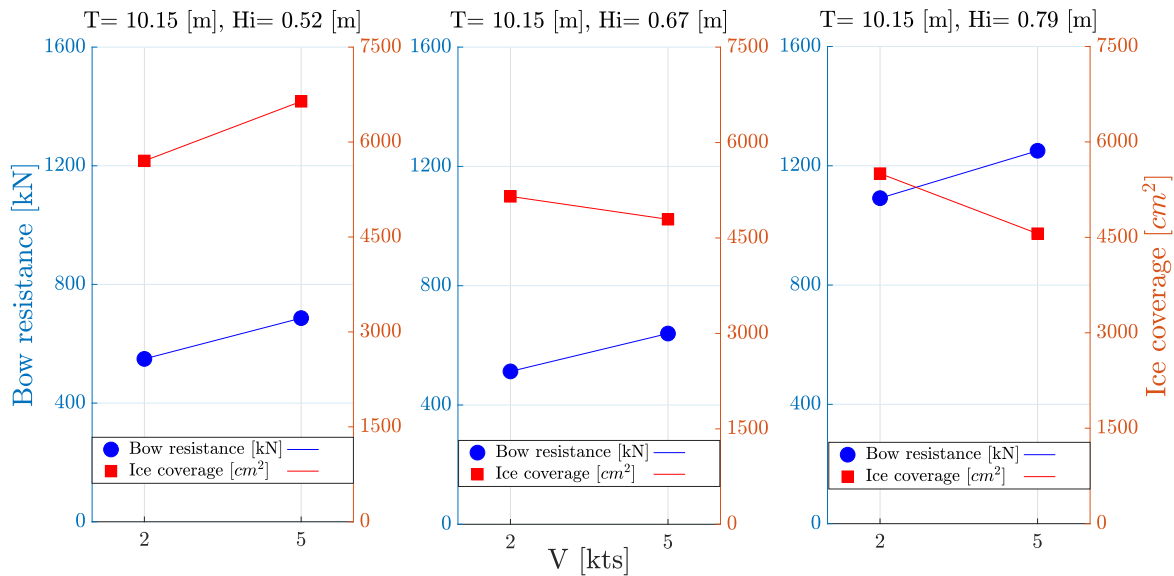


Figure 3.13: Bow resistance - ice coverage depending on model speed, $T = 10.15$ *m*

Regarding Figure 3.13, bow resistance changes in upward direction for each level ice thickness as model speed increases. Ice coverage for $Hi = 0.52$ *m* seems to be still in consistency with bow resistance for this condition. Nevertheless this correlation is not the case for $Hi = 0.67$ and $Hi = 0.79$ *m* between ice coverage and bow resistance values.

Although bow resistance and ice coverage relation seems steady for $Hi = 0.52$ *m*, such steadiness is not observed for remaining level ice thickness values tested either for $T = 5.15$ *m* or for $T = 10.15$ *m*. Thus a generalized inference regarding bow resistance/ice coverage relation can not be deduced based on given speed variation.

For bow resistance, more specifically at stem, other phenomena such as waterline angles, crushing load as well as pressure zones at contact area depending on level ice properties may cause these differences from image analysis results. Indeed, each parameter have their own influence over the ice floe formation. However, dependency of those parameters between each other should be kept in mind.

Chapter 4

CONCLUSION

In this thesis, underwater recordings of model ice tests were analyzed within the frame of a research which aims to determine ship - ice interactions for reference design having non-typical ice breaking bow shape. Preparation of the experimental setup and model tests were carried out earlier by HSVA. Image analysis methods according to the given experimental outcomes then developed specifically for this study and used to perform the visual observations.

Initially, image analysis scripts were developed based on the necessary improvements in raw images extracted from underwater recordings. Following the verification of the tool, the underwater images were classified according to the tested parameters to be used as input data in the algorithm.

Model tests are composed of six test runs in which each of three level ice thickness were tested for two loading scenarios. Each image to be analyzed resulting from these model tests were picked from a safe interval within data recorded based on model speeds tested. Due to the time lag between data measurement tables and video footage, a straightforward approach was made in order to synchronize these safe intervals with video footage. This was carried out observing the synchronization signals installed on model which indicate beginning/ending moments of measurements.

Essential physical information regarding the ice floes forms basis of visual observations made in this study. Thus, image segmentation and the information for the algorithm to return after that were scripted into the algorithm. Although feature detection has worked as it was supposed to, test environment and nature of the ice breaking event related difficulties made some manual work necessary. Some individual ice floes may stick together after ice breaking processes and it was observed that the algorithm could be misled in such

cases where contrast differences between pixels on the ice floe edges are not sufficient. Air bubbles coming from bottom of the ice tank to the surface also observed to cause likewise effect. User assessment over each analyzed image as well as the previous and next images was done manually in order to avoid these random and spontaneous nature of the environmental challenges.

It was seen by performing a convergence study that analyzing four images within safe intervals for each model speed gives sufficient accuracy. Increasing number of images analyzed would indeed improve the results. However, it was seen that good level of consistency in general characteristics of test parameters has reached for each group analyzed.

Image analysis gives pixel wise information in return for input image. Therefore a unit transform between pixel wise units and metric system was performed for each output data. For this, geometrical features of the model and image properties were used. Reprojection errors of the ice floes' sizes resulting from 3D features, predominantly hull geometry, is not corrected in this study. Therefore a margin of error between actual ice floes formed and observed could be expected.

Effect of the test parameters over ice floes as well as of the hull geometry over ice breaking process itself compared based on the analysis resultants. Comparisons based on the quantitative analysis of the ice floes between higher and lower draught scenarios made possible to see hull normal angle effect over ice breaking process. Additionally, effect of the level ice thickness over ice floe characteristics seem to be consistent with each other. However more model speed data set could help to improve the understanding of model speed effect over ice floe characteristics as level ice thickness changes.

As results from this study is compared with the results from resistance experiments done by HSVA, it was seen that ice floe size trends and bow resistance trends resemble each other fairly. Since experimental resistance study carried out by HSVA showed that the bow resistance covers about 80% of the total resistance, this resemblance may be an interesting outcome. However ice coverage and bow resistance relation seemed to be unclear based on the data set analyzed in this study.

Chapter 5

FUTURE IMPROVEMENTS

Input data given by HSVA was subjected to analysis throughout in this study. There are possible improvements for further studies which can make improvements in results obtained from this study.

An important improvement can be made by increasing the data set for parameters. Analyzing more model speed data can provide more insight by means of giving more speed dependent change. Moreover, increasing the number of images analyzed per model speed tested may lead to possible improvements in scatter.

Secondly, a modification in the algorithm in order to make detecting tiny ice particles possible would lead to improved results. Although physical interaction between these particles and hull as they move along the model may not be as influential as much as ice floes' with certain thickness are, more precise ice coverage information can be obtained.

It was mentioned in earlier sections that coordinates of the ice floes are already possible to obtain and are already stored as images were analyzed. This information is already available with respect to the local coordinate system. Transforming this local coordinate system to a global coordinate system by modifying the algorithm can enhance the usefulness of this information. Such an improvement might track certain ice floes over the model hull from one image to another as well as make local groupifications possible within the ROI.

Finally, a correction factor can be placed into the algorithm in order to minimize the projection error caused by camera position and hull geometry. By doing this, a slight but not steady increase in the size of the ice floes can be expected upwardly.

Chapter 6

ACKNOWLEDGEMENTS

First of all, I would like to express my gratitude to my professors Prof. Dr. Patrick Kaeding, Prof. Dr. Robert Bronsart, Prof. Dr. Philippe Rigo and Dr. Thomas Lindemann who supported my personal and technical development continuously throughout this master program. I would also like to thank people working at International Relations both in Liege and Rostock, they were always ready to help us selflessly.

My sincere thanks also goes to my supervisors at HSVA, Dr. Daniela Myland and Quentin Hisette who let me make use of their precious experiences and great knowledge. Needless to mention that this study would not be possible without them. They were always constructive and insightful for me when I needed their expertise. I can not pass over the friendly people at HSVA who were always gentle to me. Additionally, special thanks to the Office of Naval Research (ONR) whose financial support under the framework of the research project “Basic ship-ice interaction study” (award number N62909-18-1-2119) is gratefully acknowledged.

Additionally and importantly, I would like to thank my friends in 9th cohort from all corners of the world who reconsoladated my belief in solidarity. I will always remember their support, not only the support given to me but also the supporting between each other.

Last but not the least, I would like to thank my family, my parents and to my sister, for supporting me spiritually throughout writing this thesis and my life in general.

References

- [1] P. Ge and J. Matthews. “Sensitivity Analysis of Arctic Sea Ice Extent Trends and Statistical Projections Using Satellite Data”. In: *Remote Sens* 10 (2018), p. 230 (cit. on p. 1).
- [2] Y. Aksenov. “On the Future Navigability of Arctic Sea Routes: High-Resolution Projections of the Arctic Ocean and Sea Ice”. In: *Marine Policy* 75 (2017), pp. 300–317 (cit. on pp. 2, 3).
- [3] C. R. Service. “Navy DDG-51 and DDG-1000 Destroyer Programs: Background and Issues for Congress”. In: (2020) (cit. on p. 3).
- [4] K. Riska. “Design of Ice Breaking Ships, ILS Oy, Helsinki, Finland and University of Science and Technology, Trondheim, Norway,” in: (2006) (cit. on pp. 4, 7).
- [5] C. Carey. *Icebreaker Cruise to Antarctica - Guide to Icebreakers*. 2019. URL: https://www.chimuadventures.com/blog/2017/10/icebreaker-cruise-antarctica/?utm_campaign=shareaholic (cit. on p. 4).
- [6] K. Riska. “Ship-Ice Interaction in Ship Design: Theory and Practice, ILS Oy, Helsinki, Finland and University of Science and Technology, Trondheim, Norway”. In: (2006) (cit. on p. 5).
- [7] I. Poznyak and B. Ionov. “The Division of Icebreaking Resistance into Components”. In: *Proc. of 6th STAR Symposium, SNAME, New York* (1981), pp. 249–252. (Cit. on p. 5).
- [8] K. Riska. “Ice Action on Ship Hull”. In: *Encyclopedia of Maritime and Offshore Engineering* (2017) (cit. on p. 6).
- [9] B. Johansson and E. Mäkinen. “Icebreaking Model Tests; Systematic Variation of Bow Lines and Main Dimensions of Hull Forms Suitable for the Great Lakes”. In: *Marine Technology, SNAME* 10.3 (1973) (cit. on p. 8).
- [10] D. Sodhi. “Northern Sea Route Reconnaissance Study. A Summary of Icebreaking Technology. CRREL, Special Report”. In: (1995) (cit. on p. 8).

- [11] D. Myland and Q. Hisette. “Experimental investigations on the level ice resistance of ships with non-typical icebreaking bow shapes”. In: *International Conference on Ships and Offshore Structures ICSOS* (2020) (cit. on p. 8).
- [12] A. Group. *China’s first home-built icebreaker: carving a polar niche*. 2018. URL: <https://new.abb.com/news/detail/10000/chinas-first-home-built-icebreaker-carving-a-polar-niche> (cit. on p. 9).
- [13] U. N. O. of Information. *Navy Collaborates With Industry to Double-Dock Destroyers*. URL: <https://www.navy.mil/Press-Office/Press-Releases/display-pressreleases/Article/2237370/navy-collaborates-with-industry-to-double-dock-destroyers/> (cit. on p. 9).
- [14] G. L. Aktiengesellschaft. “Rules for Classification and Construction, I - Ship Technology, Part 0 - Classification and Surveys”. In: *Guidelines for the Construction of Polar Class Ships* (2008) (cit. on p. 10).
- [15] Q. Zhang and R. Skjetne. “Image Processing for Identification of Sea-Ice Floes and the Floe Size Distributions”. In: *IEEE Transactions on Geoscience and Remote Sensing* 53.5 (2015), pp. 2913–2924 (cit. on p. 11).
- [16] D. Myland. “Experimental and Theoretical Investigations on the Ship Resistance in Level Ice”. In: *Norwegian University of Science and Technology, Doctoral theses at NTNU;2019:198* (2019) (cit. on p. 12).
- [17] H. H. S.-V. GmbH. *Ice Tank*. 2020. URL: <https://www.hsva.de/our-facilities/ice-tank.html> (cit. on pp. 13, 14).
- [18] H.-H. S.-V. GmbH. 2020. URL: <https://www.hsva.de/our-services/model-testing/tests-in-the-ice-tank.html> (cit. on p. 14).
- [19] Q. Hisette and D. Myland. “METHODOLOGY TO INVESTIGATE THE ICE-BREAKING PROCESS OF SHIPS WITH NON TYPICAL ICEBREAKING BOW SHAPES”. In: *Proceedings of the ASME 39th International Conference on Ocean, Offshore and Arctic Engineering* (2020) (cit. on pp. 17, 19).

- [20] S. van der Walt, J. L. Schonberger, J. Nunez-Iglesias, F. Boulogne, J. D. Warner, N. Yager, E. Gouillart, T. Yu, and the scikit-image contributors. *scikit-image: image processing in Python*. June 2014. URL: <https://doi.org/10.7717/peerj.453> (cit. on p. 24).
- [21] D. Carpentry. *Image Processing with Python*. URL: <https://datacarpentry.org/image-processing/> (cit. on p. 24).
- [22] R. Rahmat, T. Chairunnisa, D. Gunawan, and O. Sitompul. “Skin Color Segmentation Using Multi-Color Space Threshold”. In: (2016) (cit. on p. 25).
- [23] V. Da Silva. *Computer Vision for Busy Developers: Finding Edges*. 2019. URL: <https://medium.com/@vad710/cv-for-busy-developers-finding-edges-836aa58e0bb5> (cit. on p. 27).
- [24] A. Chadha and N. Satam. “A Robust Rapid Approach to Image Segmentation with Optimal Thresholding and Watershed Transform”. In: *International Journal of Computer Applications* 65 (Mar. 2013) (cit. on pp. 31, 32).
- [25] L. Dantanarayana, G. Dissanayake, and R. Ranasinge. “C-LOG: A Chamfer distance based algorithm for localisation in occupancy grid-maps”. In: *CAAI Transactions on Intelligence Technology* 1.3 (2016), pp. 272–284 (cit. on p. 32).